

Gyroscopic destabilisation in polyatomic molecules. Rotational structure of the low-frequency bending vibrational states ν_{23} and ν_{11} of dimethylsulfoxide

Arnaud Cuisset^{a)} and Dmitrii A. Sadovskii^{b)}

Laboratoire de Physico-Chimie de l'Atmosphère, Département de physique,
Université du Littoral – Côte d'Opale, 59140 Dunkerque, France

(Dated: 10 May 2013 at 14:09; submitted on February 20, 2013, in final form on May 3, 2013)

We give details of the spectroscopic observation of the gyroscopic destabilisation in the ν_{23} vibrational state of dimethylsulfoxide (DMSO) announced by Cuisset, Pirali, and Sadovskii in [Phys. Rev. Lett. **109**, 094101 (2012)]. Following the first successful high-resolution spectroscopic study of the rotational structure of the “perpendicular” band of DMSO at 324 cm^{-1} associated with the ν_{23} bending vibrational mode, the rare subsystem of the ν_{23} rotational levels consisting of a series of four-fold quasidegenerate levels (4-clusters) was identified. Our complete analysis of the underlying rotational dynamics uncovered a bifurcation leading to the gyroscopic destabilisation of one of the two stable principal axes of inertia, a phenomenon known previously only in a few triatomic molecules.

PACS numbers: 33.20.Ea, 33.20.Vq, 33.15.Mt

Keywords: synchrotron FTIR spectroscopy, THz radiation, vibration-rotation spectrum, bending mode, accidental symmetric top, effective rotational Hamiltonian, axis of stationary rotation, rotational energy level clusters, bifurcation

I. INTRODUCTION

Dimethylsulfoxide (DMSO), a relatively common sulphur compound, is sensibly present in nature and is widely used in industry, health care, and research. Up until most recently^{1–3}, detailed information on its low frequency vibrations was unavailable due to its low vapor pressure that made conventional light sources in the far infra-red (FIR) regions ineffective for high-resolution spectroscopic studies.

In this paper, we give details of the first successful analysis³ of the rotational structure of the OSC_2 frame bending fundamental vibrational state ν_{23} of DMSO whose high-resolution gas phase absorption spectrum was observed along with that of ν_{11} by Cuisset *et al.*^{1,2} using the AILES beamline of the SOLEIL synchrotron source^{4,5}. The exceptional properties of the synchrotron radiation in the FIR domain near 350 cm^{-1} were absolutely crucial to these experiments. The analysis was complicated by a large number and high density of spectral lines and had to account for the specific spectral structures reflecting the accidental closeness of DMSO to the symmetric top.

Our results have three principal aspects. We have responded to the necessity of completing the information on the vibration-rotation constants of this molecule when the opportunity came. We have analyzed the obtained rotational constants in order to uncover the corresponding interesting classical rotational dynamics with additional stationary axes of rotation. Furthermore, our information on the individual FIR absorption lines of

DMSO are of considerable interest to monitoring concentrations of this molecule⁶.

A. The phenomenon of the gyroscopic destabilisation

In this paper we focus on the second group of results, notably on the phenomenon of gyroscopic destabilisation that we observed in DMSO. It can be described briefly as follows. At low amplitude j of the total angular momentum⁷ \mathbf{j} , this molecule rotates similarly to an oblate slightly asymmetric Euler top with principal moments of inertia $I_A < I_B \ll I_C$. Specifically, its principal axes of rotation A and C are stable⁸ and quantum states corresponding to the precession about them form “usual” doublets⁹ (or 2-clusters). When j increases and, additionally, the asymmetric bending vibrational mode ν_{23} of the OSC_2 frame is excited, the A axis loses stability in a pitchfork bifurcation and two equivalent new stable axes X emerge. When the latter become sufficiently stable with increasing quantum number $J > 40$, we observe the “unusual” four-fold degenerate levels or 4-clusters formed by merging of two neighboring A -type doublets. This phenomenon was anticipated and well understood from the classical point of view in the mid-80's^{10–12} using the classical representation of molecular rotation¹³, and was previously observed only in a small number of triatomic molecules with nearly 90° bond angle^{14–17}. Similar phenomena occur in many different concrete systems, notably molecular resonant two-mode vibrations¹⁸, Bose-Einstein condensates¹⁹, and even quantum entanglement²⁰ of “spins”. They all can be analyzed within the universal concept of molecular quantum bifurcations^{18,21,22}.

^{a)}Corresponding author: Arnaud.Cuisset@univ-littoral.fr

^{b)}Contact: sadovskii@univ-littoral.fr

B. The role of the spectroscopic analysis

The experimental evidence of the gyroscopic destabilisation relies on the spectroscopic data on the rotational energy levels. The latter are reproduced using an effective Hamiltonian $\hat{H}_{\text{rot}}(\mathbf{J})$, typically a Taylor series in even degrees of the body-fixed²³ components of the angular momentum vector operator $\mathbf{J} = (J_a, J_b, J_c)$ whose phenomenological parameters are adjusted to reproduce the frequencies of the observed spectral lines to the experimental accuracy. In our case here we study the FIR absorption transitions $|0\rangle \rightarrow |\nu_{23}\rangle$ (and $|0\rangle \rightarrow |\nu_{11}\rangle$) to the ground state with accuracy of about $1.5 \times 10^{-4} \text{ cm}^{-1}$. Subsequently, the Hamiltonian \hat{H}_{rot} is used to reconstruct the entire rotational energy spectrum, including those levels which—for some reasons—have not been involved in the assigned experimental transitions, and to extrapolate to higher values of J . This allows for the new experimental lines to be assigned and the parameters of \hat{H}_{rot} , extended, if necessary, to higher degrees in (J_a, J_b, J_c) , to be refitted for a better agreement with experiment.

At this point, it is important to note that up to 85% of the $|\nu_{23}\rangle$ rotational levels are C -type doublets, the share of the A -type doublets amounts to 10–12% and the X -type quadruples constitute only a tiny fraction of all states. Consequently, a very consistent state-of-the-art effort is required to either observe transitions involving these quadruples, or, at least, to accumulate sufficient evidence that the Hamiltonian \hat{H}_{rot} predicting their existence is sufficiently stable and the prediction is not a mere artifact of improper extrapolating a power series. In the present study we claim to achieve both objectives. Out of total of more than 7500 individual $|0\rangle \rightarrow |\nu_{23}\rangle$ transitions²⁴ with J up to 60, we were able to assign more than 550 lines involving most of the A -states and about 70 transitions from the X -quadruples. Furthermore, the quadruplets, that we described, belong to the interval of J where \hat{H}_{rot} is supported directly by the experimental data both in the prevailing C -part, the smaller A -part of the energy spectrum and some of the X -states at the high energy end of the multiplet. We provide further essential details in Sec. II.

C. The dynamical analysis

To understand the dynamical meaning of the 4-cluster formation and to uncover the phenomenon of the gyroscopic destabilisation we turn to the classical limit of our system⁷ and study its dynamics (Sec. III). The classical rotational energy $\mathcal{H}_{\text{rot}}(\mathbf{j})$ of the molecule in an isolated nondegenerate vibrational state, such as, for example, the ground state $|0\rangle$, is obtained after replacing the components (J_a, J_b, J_c) of the angular momentum operator \mathbf{J} for their classical analogs⁷:

$$\mathbf{J} \mapsto (j_a, j_b, j_c) = j (\sin \theta \sin \phi, \sin \theta \cos \phi, \cos \theta).$$

The amplitude j and the world orientation of the total angular momentum \mathbf{j} are conserved. The set of points representing all instantaneous body-fixed orientations of the classical rotation axis and two possible directions of rotation for a given j is a sphere \mathbb{S}_j^2 which embeds in $\mathbb{R}_{(j_a, j_b, j_c)}^3$ as a 2-sphere of radius j . This space is a phase space of the classical one-degree-of-freedom dynamical system with Hamiltonian \mathcal{H}_{rot} . This system can be viewed as a nonrigid reduced Euler top system. Its equilibria given by the stationary points of \mathcal{H}_{rot} represent the stationary rotation axes of the molecule.

Fixing angular momentum amplitude j , we can visualize^{13,18} the function $\mathcal{H}_{\text{rot}} : \mathbb{S}_j^2 \rightarrow \mathbb{R}$ as a *closed surface in \mathbb{R}^3* using spherical angles (θ, φ) to define the axis and the direction of rotation and using the distance from the origin to give the value of \mathcal{H}_{rot} (see Sec. II B). This representation makes the analysis particularly straightforward. The surface inherits the symmetries²⁵ of \mathcal{H}_{rot} , and in particular, it is \mathbf{j} -inversion invariant, so that any axis is represented on it by two equivalent opposite points corresponding to two rotation directions about this axis.

The lowest order $\mathcal{H}_{\text{rot}}^0$ is quadratic in \mathbf{j} . It describes the reduced motion of a rigid Euler top. Higher orders give effective corrections due to the nonrigidity of the molecule. They describe specific deformations of the averaged geometry and dynamical responses provoked by the centrifugal forces. The increased relative importance of these orders at large j can result in qualitative changes in the system of the equilibria of the system, and in particular—can cause the gyroscopic destabilisation. We show in Sec. III how this occurs in the case of the asymmetric ν_{23} bending fundamental vibrational state of DMSO.

It should be well understood that our analysis tells precisely “what” happens, but it does not explain “why”. Working at the level of an effective Hamiltonian with phenomenological parameters, we can uncover the classical dynamical meaning of the qualitative changes, that we observe in the rotational level spectrum. Further physical analysis requires a reliable molecular potential for (at least) the bending modes of DMSO, see Sec. III and IV. We also like to point out the general requirement for the phenomena like the loss of stability of axis A to occur and to do so at reasonably low j : the principal moments of inertia of the molecule²³ should be “accidentally” close to an exceptional more symmetric case. This is why there is only a small number of known “molecular tippe tops”, most notably the somewhat exotic triatomic molecules^{15,17,26} H_2Se and H_2Te , whose almost 90° bond angle turns them into accidental symmetric tops. DMSO provided the first example in larger molecules.

II. ROTATION-VIBRATION STATES OF DMSO

DMSO is a ten atomic C_s symmetric²⁸ molecule whose equilibrium configuration with the O–S bond in the symmetry plane is shown in Fig. 1. The OSC_2 frame bending

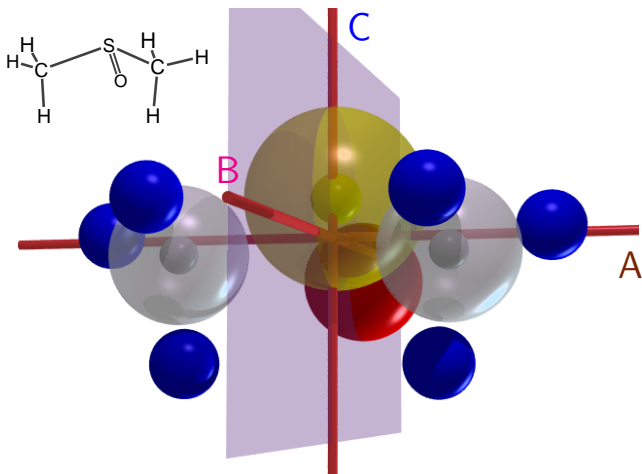


FIG. 1. Schematic representation of the equilibrium configuration of $(\text{CH}_3)_2\text{SO}$ (DMSO) according to *ab initio* computations²⁷; the three principal axes of inertia cross at the center of mass, axes B and C (vertical) lie in the symmetry plane. Reproduced from Refs. 2 and 3.

vibrations of DMSO can be easier understood qualitatively after replacing the methyl groups CH_3 by single bulky atoms and considering a non-planar four atomic molecule. Furthermore, to model the absorption spectrum selection rules we can take into account that atoms O and S are highly polarized while the combined charge on the methyls is nearly zero. The harmonic force field of DMSO was determined by Typke and Dakkouri²⁹ in 2001 using liquid phase data for the low frequency bending modes, and using vibrational satellite bands in the microwave (MW) region for the internal rocking modes. Typke and Dakkouri²⁹ also derived the average equilibrium configuration (Fig. 1) after combining all available data from IR, Raman and MW spectroscopy with gas electron diffraction data and *ab initio* predictions and reevaluating the harmonic force field of the molecule.

At low vibrational excitations, the methyls cannot rotate internally about the $\text{S}-\text{C}$ bonds and the vibrations of the molecule can be described in terms of 24 normal modes²⁹. Among them, the symmetric (A' -type) ν_{11} and ν_{12} and the asymmetric (A'' -type) ν_{23} modes with frequencies of $300\text{--}350\text{ cm}^{-1}$ represent the bending vibrations of OSC_2 . We study ν_{11} and ν_{23} which involve respective significant in- and out-of-symmetry-plane displacements of the O atom and, as a consequence, induce sufficiently large dipole moments and are well visible in the FIR absorption spectra¹. The ‘‘FIR dark’’ mode ν_{12} is primarily a symmetric reciprocal motion of the uncharged methyls and has a very small induced dipole. The only hope to find ν_{12} in the absorption spectrum is due to its Coriolis interaction with ν_{23} and/or ν_{11} . For a complete description of the low frequency vibrations of DMSO, we should mention the two ‘‘torsional’’ modes which correspond to the internal rocking of the methyls with frequencies near 200 cm^{-1} . These modes are also

inactive in the FIR absorption spectrum. All other vibrational modes of DMSO have significantly larger frequencies and can be ignored in our context.

DMSO is a slightly asymmetric top molecule with two nearly equal rotational constants $A \gtrsim B$, and significantly smaller third constant C . Its asymmetry, represented by the Ray parameter

$$\kappa = \frac{2B - (A + C)}{A - C} \approx 0.91, \quad (1)$$

approaches that of an *oblate* symmetric top ($\kappa = 1$). This specificity of DMSO was mentioned in Ref. 29 and the example of DMSO was used to discuss K -doubling and Watson’s S -reduction^{29–31}. To appreciate how close the molecule is to the symmetric top limit, imagine³² switching the ^{16}O atom for its isotope ^{17}O or ^{18}O . In the usual DMS^{16}O (fig. 1), axis A with the minimal moment of inertia, is *perpendicular* to the symmetry plane. DMS^{17}O is a nearly perfect symmetric top, and in DMS^{18}O , axes A and B are interchanged, and A lies *in-plane*.

A. Experimental data

At room temperature, the saturated vapor pressure of DMSO is weak: at 293K it is only 0.42 Torr , about 40 times less than that of water. Such low volatility calls for maximum sensitivity in high-resolution gas-phase spectroscopic experiments.

1. Ground state information from the microwave spectra

The analysis of the ground state MW transitions of DMSO^{29,33} allowed to determine quartic centrifugal distortion constants. Most comprehensively, to $J = 50$, the ground state has been recently re-analyzed in Ref. 34. The MW data are several orders of magnitude more accurate than the FIR measurements and we depend on them for fixing the ground state rotational constants and for assigning most of our observed individual rovibrational $|0\rangle \rightarrow \nu_{23}$ transitions through the ground state combination differences (Sec. II E 2).

2. Rotation-vibration spectra

Until the work by Cuisset *et al.*¹ in 2010 that took full advantage of the exceptional properties of the AILES beamline of SOLEIL in the THz/FIR domain^{4,5}, the last reported gas phase rovibrational spectra of DMSO went back more than thirty years³⁵ and were limited to low resolution and wavenumbers above 600 cm^{-1} . Preliminary measurements performed at low resolution with the internal sources of the IFS125 Bruker FTIR spectrometer updated the vibrational frequencies of all IR active modes of DMSO (cf fig. 2 and Table IV) and gave a better agreement with the force field in Ref. 29.

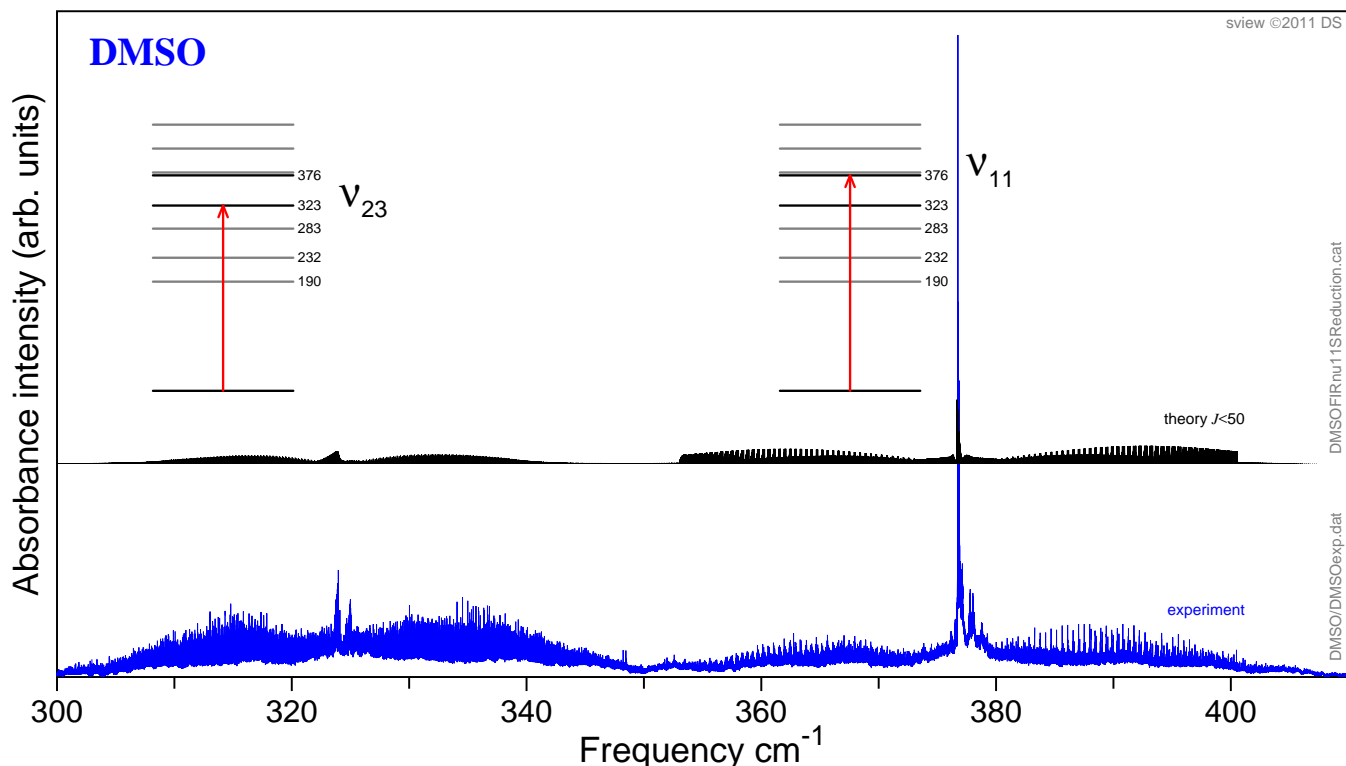


FIG. 2. Spectrum (lower trace, blue) of the ν_{23} and ν_{11} fundamental bands of DMSO observed using the AILES beamline of the SOLEIL synchrotron ($P = 0.06$ Torr, $L = 150$ m, $\Delta\nu = 0.00015$ cm^{-1} , 700 scans, 46 hours of acquisition) by Cuisset *et al.*^{1,2} and predicted transitions (stick spectrum, upper trace, black). The amplitude scaling of the two traces is independent; the experimental unresolved ν_{11} Q -branch takes nearly the full height of the plot. The inserts (top) represent the lowest vibrational energy levels of DMSO in cm^{-1} according to our measurements for ν_{11} and ν_{23} and the harmonic frequencies computed by GAUSSIAN²⁷. Gray lines represent dipole inactive states and their overtones, arrows show the transitions analyzed in this work.

The FIR absorption spectrum of DMSO (fig. 2) which we use in this work were recorded in the 50–650 cm^{-1} spectral range on the THz/FIR beamline AILES of the SOLEIL synchrotron source. Due to the natural high brilliance and the small divergence of the synchrotron radiation (SR) in this domain, the acquisition time of the rovibrational spectra can be drastically reduced³⁶. Using SR was absolutely essential in order to observe, in a limited time, the resolved rovibrational FIR spectrum of DMSO^{1,2}. AILES was designed to obtain exceptional performances in terms of flux, spectral range, and stability in the entire IR spectral domain; its reliable high resolution spectroscopic ensemble⁴ has high detection sensitivity. In comparison to conventional thermal sources, such as the Hg discharge lamp, the most gain from the use of SR was obtained in the THz/FIR domain. Thus the delivered flux and the achieved S/N ratio for the 100 cm^{-1} SR were found 10 times larger⁵. Opened to external users at the end of 2008, AILES has demonstrated its exceptional suitability for gas phase high resolution THz spectroscopy³⁷, which for the most part could not be performed with thermal sources.

In our experiments, the AILES beamline was focused onto the entrance aperture of a high resolution Bruker

IFS 125 Fourier transform interferometer containing a 6 μm mylar-Silicon composite beamsplitter suitable for the THz spectral range. To limit absorption by the atmospheric compounds, the interferometer was evacuated continuously to 10^{-5} Torr. The He-cooled silicon bolometer detector was equipped with an optical 10–600 cm^{-1} band-pass filter. The sensitivity was boosted by using a White type multipass cell which was adjusted to a 150 m optical path length and was isolated from the interferometer by 50 μm thick polypropylene windows. DMSO of stated purity higher than 97% from Aldrich Chemical Co was used without further purification. Its saturated vapor at room temperature was injected directly in the cell.

The FIR spectrum of DMSO (Fig. 2) was recorded at 0.06 Torr with 0.0015 cm^{-1} resolution. The Fourier transforms of 700 interferograms were co-added to achieve the larger-than-100 S/N ratio. The total acquisition time amounted to 46 hours. Note that it would have taken half a year to achieve a similar S/N ratio with a conventional source. The spectrum in Fig. 5 was calibrated using residual water absorption lines with known wavenumbers³⁸. This gave the RMS calibration accuracy of about 1.5×10^{-4} cm^{-1} .

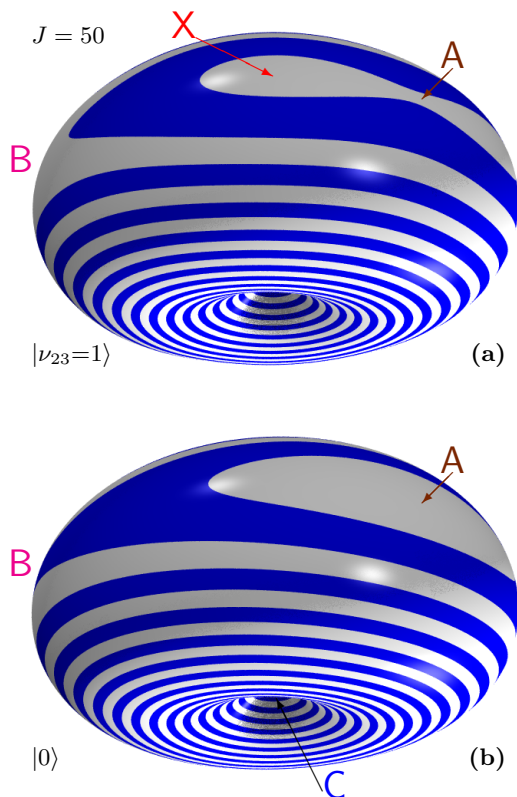


FIG. 3. Classical rotational energy of DMSO in the ν_{23} fundamental vibrational excited state (a) and the ground state (b) with angular momentum $J = 50$. The surfaces are drawn in slightly rotated coordinates (J_a, J_b, J_c) of Fig. 1. In both plots, the energy is given, up to the same fixed additive constant and scale, by the radial distance from the origin as function of the position of the instantaneous axis of rotation. Equidistant sets of constant energy are stripe painted to display more clearly the shape of the surfaces. We see a deep minimum along the J_c axis (vertical) and very shallow height variations in the equatorial area. Adapted from Ref. 3. The animation `DMSOsRE-animj.gif`²⁴ illustrates the evolution of the rotational energy of ν_{23} as J varies on the interval $[30, 60]$.

B. Rotational structure and spectra of DMSO

For low rotational excitations, i.e., for a given sufficiently small quantum number J , the system of the rotational levels of DMSO can be well approximated by the spectrum of a slightly asymmetric oblate top with two usual series of rotational state doublets⁹, specifically, one large series of C -states ascending from the minimal energy of J -multiplet, and one much smaller series of A -states descending from the maximal energy. The two series meet in the transitional energy domain corresponding to the classical rotation about axis B .

Figure 3(b) illustrates the classical rotational energy of DMSO in the ground state $|0\rangle$, which is obtained using the classical analog $\mathcal{H}_{\text{rot}}(\theta, \phi; j)$ of the rotational Hamiltonian (see Sec. IC) with parameters in Table I. We can see that most of the reduced rotational phase space \mathbb{S}_j^2

is taken up by stable rotation about axis C (concentric stripes in Fig. 3), which correlates to the motion in the oblate symmetric top limit. Rotations about axis A are represented by a much smaller domain of \mathbb{S}_j^2 (white area near axis J_a in the equatorial belt of the surface), and a similarly small domain (self-intersecting blue stripe in Fig. 3) corresponds to delocalized unstable motion with intermediate energies.

In the simplest rigid rotor approximation, the number of A -states relative to the number of all states with a given J , is approximately:

$$\frac{2}{\pi} \arcsin \varepsilon = \frac{2}{\pi} \arcsin \sqrt{\frac{A-B}{A-C}} \approx 0.14.$$

So the number of the A -type doublets of DMSO can be estimated as $\approx 0.14 J$ and they exist only for $J > 8$. The C -states, constituting up to 85% of all rotational states, correlate with the oblate symmetric top levels and are classified adequately by the good quantum number $K = K_c$ or the projection J_c of \mathbf{J} on axis C . For this reason, C is the most natural choice of the quantization axis for the rotational basis functions $|J, K\rangle$ used to represent the matrix of the effective rotational Hamiltonian $H_{\text{rot}}(\mathbf{J})$.

C. Effective rovibrational Hamiltonian

In our analysis, we attempted describing the $|\nu_{11} = 1\rangle$ and $|\nu_{23} = 1\rangle$ fundamental vibrational states in two ways: either as two isolated, or as two interacting states. In the first case (Sec. IIC1), we considered no explicit rotation-vibration interactions between them or with other close lying states, and no vibrational resonance, such as the Fermi resonance with the $|\nu_{24} = 2\rangle$ overtone (cf Fig. 2 and Ref. 29). In the second case, we included explicit first-order Coriolis interaction terms (Sec. IIC2).

1. Isolated state model

The effective rotational Hamiltonian for an isolated vibrational state $|v\rangle$ with frequency ω ,

$$H_{\text{rot}} = \omega + (A + \delta_v A) J_x^2 + (B + \delta_v B) J_y^2 + (C + \delta_v C) J_z^2 + \dots,$$

includes purely rotational terms describing the ground state $|0\rangle$ and their corrections δ_v in the upper state $|v\rangle$. Recall that in order to minimize the number of independent adjustable parameters of the higher order terms in H_{rot} , the latter is reduced to one of the D_2 -symmetric forms introduced by Watson³⁹. For nearly symmetric tops, it is customary^{29-31,40} to use the s -form, with axis C , the axis of the oblate symmetric top limit for DMSO, chosen as quantization axis z . Near the symmetric top limit, the s -form requires a smaller reduction transformation, and so is, in principle, a faster converging series. Additionally, we may also expect a lesser distortion of the original dipole moment operator. In other words,

TABLE I. Vibration-rotation parameters (MHz) of the effective Hamiltonian of DMSO in the model of isolated vibrational states; the value of a parameter for the vibrational state ν_k equals the sum of values in columns $|0\rangle$ and ν_k , e.g., $A_{|\nu_k\rangle} = A + \delta_k A$

Parameter	$ 0\rangle$	ν_{11}	ν_{23}	Order
$\omega \times 10^{-6}$	0*	11.294723808(116)	9.712918100(95)	THz
A	7036.5821413(235)	5.01169(50)	0.86894(43)	MHz
B	6910.8300483(228)	3.59040(48)	-6.86687(41)	MHz
C	4218.776469(44)	-1.02354(75)	11.97998(57)	MHz
$-D_K \times 10^3$	-3.989611(48)	0.18179(164)	-0.39630(105)	kHz
$-D_{JK} \times 10^3$	8.937700(49)	-0.42873(143)	0.57425(99)	kHz
$-D_J \times 10^3$	-6.0889430(164)	0.32897(45)	-0.49427(34)	kHz
$d_1 \times 10^3$	-0.1639895(103)	0.061798(229)	3.818801(214)	kHz
$d_2 \times 10^3$	-0.2717085(58)	0.027806(150)	-7.220016(114)	kHz
$H_K \times 10^6$	-0.0218391(256)	-0.04619(166)	0.08931(98)	Hz
$H_{JKK} \times 10^6$	0.052731(37)	-0.04977(200)	-0.31066(121)	Hz
$H_{JJK} \times 10^6$	-0.0395737(242)	0.11876(117)	0.03837(74)	Hz
$H_J \times 10^6$	0.0088379(81)	-0.08128(33)	0.104666(233)	Hz
$h_1 \times 10^6$	-0.0017702(63)	-0.015379(125)	-0.511893(113)	Hz
$h_2 \times 10^6$	0.0010721(51)	-0.001259(94)	1.288897(108)	Hz
$h_3 \times 10^6$	-0.00137497(225)	-0.002841(51)	1.882505(45)	Hz
$L_K \times 10^9$	-0.0001288(60)	0.21217(88)	-0.20742(49)	mHz
$L_{KKJ} \times 10^9$	0.0004235(116)	-0.34791(128)	0.45905(75)	mHz
$L_{JK} \times 10^9$	-0.0004527(104)	0.25430(100)	-0.23035(56)	mHz
$L_{JJK} \times 10^9$	0.0001845(57)	-0.09788(51)	0.009084(300)	mHz
$L_J \times 10^9$	-0.00001071(174)	0.021496(128)	0.001536(90)	mHz
$l_1 \times 10^{12}$	0.03231(181)	6.094(32)	-9.2911(284)	μ Hz
$l_2 \times 10^{12}$	-0.02464(161)	3.3008(305)	-62.235(38)	μ Hz
$l_3 \times 10^{12}$	0.01545(92)	3.0986(192)	2.7548(164)	μ Hz
$l_4 \times 10^{12}$	0*	1.1313(66)	0.5362(49)	μ Hz

such choice is the most physical for DMSO. These aspects can be especially helpful at the initial stages of the spectroscopic analysis and for high- J extrapolations.

In practice, however, the situation is less straightforward. In addition to a pure scalar series in J^2 , the s -form Hamiltonian includes diagonal and tensorial terms. The former are various powers of J^2 and K^2 (or $\cos^2 \theta$ in the classical limit \mathcal{H}_{rot}) and contribute primarily to the energies of the C -states, while the latter include also the powers of $(J_a \pm iJ_b)^2$ (or $\sin^2 \theta$) that describe the A -states or the intermediate states. The number of terms of each kind is roughly equal, while the number of C states is much larger. This disproportion may result in stronger correlations between the tensorial terms, especially when the A -states are observed with lower precision or not observed at all. In such cases, the a -form may appear more stable³⁴. Since the purpose of this work is in the uncovering of specific interesting rotational dynamics and not a mere fitting of the experimental data, we kept the s -form of H_{rot} , making a considerable effort to observe sufficiently many transitions to the A -states in order to stabilize the least square fit. In particular, we assigned practically all transitions²⁴ involving the A -states of $|\nu_{11} = 1\rangle$ up to $J = 55$, and a sufficiently large number of A and X states of $|\nu_{23} = 1\rangle$.

2. Coriolis interactions

The overlap of the rotational structures of $|\nu_{23} = 1\rangle$ and $|\nu_{11} = 1\rangle$ that occurs for $J > 25$ (cf Fig. 9) may suggest to account explicitly for the principal order (linear in J) Coriolis interaction⁴¹ using non-diagonal terms

$$\zeta_\xi (a_{23}^\dagger a_{11} + a_{11}^\dagger a_{23}) J_\xi \text{ with } \xi = b, c. \quad (2)$$

Note, however, that the overlapping parts of rotational multiplets have levels with distant values of K_c , and the $\Delta K = 1$ interaction in Eq. (2) is important only when these levels are very close. In our case, the isolated state model turned out to be adequate within the accuracy of our data and the range of the observed J values. The introduction of $\zeta_{a,b}$ with values of about 600 MHz did not bring any sensible improvement to the fit, while large correlations between A , B , C , and $\zeta_{a,b}$ did not justify an interacting state model. Furthermore, with these values of $\zeta_{a,b}$, the maximal level mixing of ν_{11} and ν_{23} is about 0.1%, which excludes any visible spectral intensity modifications.

D. Transition moments and selection rules

Because the rotational constants A and B of DMSO are very close, the absorption spectrum of this molecule

has structures reminiscent of a symmetric top spectrum. Roughly considered, the branches in the $|0\rangle \rightarrow \nu_{11}$ and $|0\rangle \rightarrow \nu_{23}$ bands (see fig. 2) of DMSO resemble those of a “parallel” and a “perpendicular” symmetric top spectrum, respectively. On the other hand, unlike any true symmetric top molecule, DMSO has no sufficiently high order, discrete, axial symmetry C_k with $k > 2$, and its dipole moment function $\mu(q)$ is very different from that of a symmetric top, see Appendix²⁴ B 1. This calls for some consideration. In this section, we survey the transition moment operators and the corresponding selection rules; related standard formulae are collected in Appendix²⁴ B.

1. Permanent and induced dipole moments of DMSO

In a symmetric top, the permanent dipole moment, if it exists, aligns with the top’s axis (our axis C), while the oscillating dipole moment can be either parallel or orthogonal to the axis, i.e., both components cannot be induced in one vibrational eigenstate and, consequently, the latter appears in the absorption spectrum as either a “parallel” (\parallel) or a “perpendicular” (\perp) rotational band.

The permanent dipole moment vector of DMSO μ^0 is invariant with respect to the symmetry plane BC (cf fig. 1), i.e., μ^0 transforms according to the irreducible representation A' , and lies in the symmetry plane of the molecule. As explained in Appendix²⁴ B 1, μ^0 is approximately aligned with the highly polarized O–S bond. Taking the smaller effective charges on CH_3 , we obtain for the two components μ_c^0 and μ_b^0 of μ^0 with respect to the principal axes of inertia an approximate ratio of 0.38.

The orientation of the first order term in the vibrationally induced dipole moment vector $\mu(q)$, which governs the fundamental transitions $0 \rightarrow 1$, is restricted by the symmetry of the vibration q : for the excitation of the anti-symmetric modes, such as $|\nu_{23} = 1\rangle$, the vector $\mu(q)$ aligns with axis A , i.e., has only one nonzero component $\mu_a(q)$; for $|\nu_{11} = 1\rangle$, this vector remains in the symmetry plane BC and has components $\mu_b(q)$ and $\mu_c(q)$. Because ν_{11} can be roughly considered as an in-plane bending vibration of the S–O fragment, the ratio of the two components μ_c/μ_b in the $|\nu_{11} = 1\rangle$ state is, approximately, the inverse of μ_c^0/μ_b^0 , see Appendix²⁴ B 1.

2. Selection rules and simple simulations

Concrete expressions for the intensities of various allowed branches in the parallel (\parallel) and perpendicular (\perp) bands of a symmetric top molecule can be found in Appendix²⁴ B 2 where Table V presents maximum intensities in these branches for DMSO in the rigid symmetric top limit at 298K. These bands are characterized by $\Delta K_c = 0$ and ± 1 , respectively, while their ΔJ can be 0 or ± 1 . Thus, the \parallel -band consists of three branches⁴² ${}^Q P$, ${}^Q Q$, and ${}^Q R$, of which ${}^Q Q$ is $2\sqrt{B/C}$ times stronger, see Table V. Among the six allowed branches of the \perp -band,

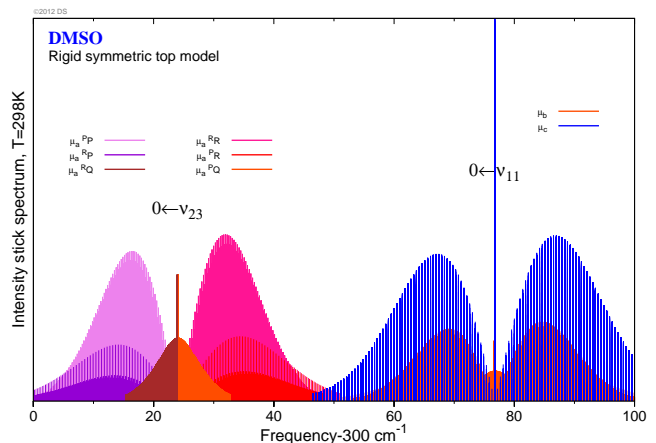


FIG. 4. Absorption spectrum of the ν_{23} and ν_{11} fundamentals of DMSO in the rigid symmetric top approximation at 298K. In the online color version, different branches of the perpendicular band $0 \rightarrow \nu_{23}$ and parallel and perpendicular components of the $0 \rightarrow \nu_{11}$ band are color coded.

the strongest are ${}^P P$ and ${}^R R$. They are slightly stronger, by factor of $\sqrt{B/C}$, than ${}^R Q$ and ${}^P Q$. Compared to that of the ${}^Q Q$ branch of the \parallel -band, their maximum is $\langle \mu_b \rangle^2 / 2 \langle \mu_c \rangle^2$ times lower. The \parallel -band is the only one to have the most compact ${}^Q Q$ branch, whose strength can be greatly amplified by its integrated intensity in the insufficiently resolved spectrum. We also note, that branches differ in the states which contribute to most intense transitions. Thus the C -states with $K_c \sim J$ dominate in the ${}^Q Q$ -branch, while transitions involving $K_c \ll J$ (eventually the A -states) are emphasized in the ${}^Q P$ and ${}^Q R$ branches.

We conclude that the $0 \rightarrow \nu_{23}$ spectrum, like any spectrum involving first excited vibrational state of an A'' -type mode, should be similar to the perpendicular band of a symmetric top. On the other hand, most of the purely rotational transitions within the same vibrational state, such as $0 \rightarrow 0$, or those to the first excited state of type A' , such as $0 \rightarrow \nu_{11}$, can be understood as a superposition of the \perp band due to $\mu_b(q)$ and the \parallel band due to $\mu_c(q)$, of which only the former is present in a symmetric top. In the rotational bands of DMSO, the \perp band, notably the ${}^R P$ branch involving large- K_c states, is factor $(\mu_b^0/\mu_c^0)^2$ stronger than the symmetric-top transitions ${}^Q R$. On the other hand, in the particular case of $0 \rightarrow \nu_{11}$, the relative intensity of the parallel component increases by factor of $(\mu_c/\mu_b)^2$. All these aspects are clearly visible in a simple rigid symmetric top model spectrum in Fig. 4. In this simulation, we computed the rotational structure using just two constants $\bar{B} = (A + B)/2$ and C , with A , B , and C of the ground state of DMSO (Table I) and the minimum set of the induced dipole moment parameters, notably $\mu_a \approx \mu_c$ and $\mu_b = 0.6\mu_c$ (see Appendix²⁴ B 1).

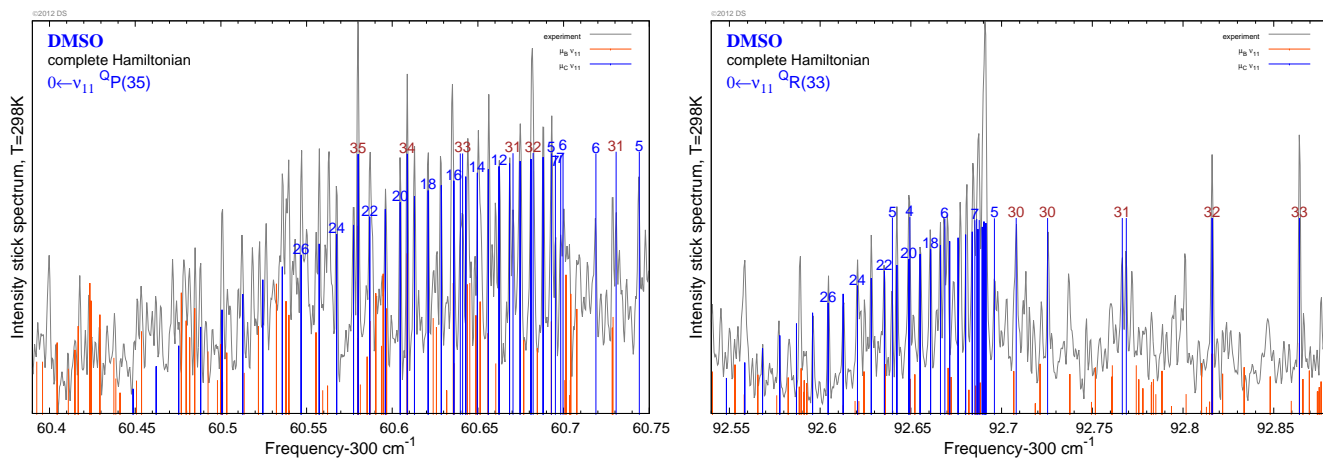


FIG. 5. Reciprocal multiplets ${}^Q P(35)$ and ${}^Q R(33)$ of the $0 \rightarrow \nu_{11}$ spectrum. Gray line shows the observed FT-FIR spectrum; blue and orange sticks mark computed intensities for dipole moment components μ_c (dominant \parallel component) and μ_b (\perp component); K_c or K_a assignments for most prominent lines are displayed on top of the sticks in blue or brown, respectively. Note that the presence of many weaker lines of other bands obscures the μ_b -transitions in this region.

E. Spectroscopic analysis

For computing and fitting the absorption spectra of DMSO we used the standard programs by Pickett^{43,44}. Working with very dense FIR spectra that contained many additional unassigned transitions, probably hot bands, required developing special computer programs in order to systematically uncover and assign the ground state combination differences. These programs were particularly important in the ν_{23} analysis, where more than 6000 lines were assigned with their aid, and elsewhere in high- J assignments. To assist and visualize assignments, we also used the programs by Kisiel^{45,46}.

We obtained the ground state parameters in Table I using the MW $0 \rightarrow 0$ assignments from Ref. 34 up to $J = 60$. They remained essentially unchanged throughout the analysis because the typical accuracy of the MW data compared to that of the FT-FIR combination frequencies is significantly higher (0.05 MHz versus about 5 MHz), and their values in Table I are close to those obtained in Ref. 34 for their s -III choice. So, we could rely on the ground state Hamiltonian H_{rot} for the combination frequency assignments of our FIR spectra. Table II summarizes the fit of the two FIR bands, and the MW transitions. Below we give essential details of the FIR band analysis.

1. The ν_{11} fundamental transition

The much simpler parallel (\parallel) component of the $0 \rightarrow \nu_{11}$ transition (Fig. 2, right) is dominant, and its resolved ${}^Q P$ and ${}^Q R$ branches constitute a good starting point of the analysis. Recall from Sec. B 2, that transitions involving low K_c are more pronounced in these branches. This allows an immediate access to the most complex part

of the rotational structure of ν_{11} (the A -states, transitional states, and the upper part of the C -state ladder). The key to assign the spectrum² is in the high-frequency end of the ${}^Q R(J)$ multiplets with sufficiently high $J = 25 \dots 40$ which shows very strong, clearly visible transitions involving the A -states, notably the outermost state with $J = K_a$, see Fig. 5 right. Entering basic rotational and dipole moment parameters, we managed to model these multiplets for $J = 12 \dots 25$ well enough for picking ground state combination frequency differences involving the reciprocal, more complex ${}^Q P(J+2)$ multiplets (Fig. 5 left), and thus making unambiguous assignments. After that, fitting the spectrum became relatively straightforward. Subsequently, it became also possible to assign a number of μ_b transitions, such as the ones shown in Fig. 6, thus accessing directly the high- K_c end of the eigenspectrum and obtaining the experimental estimate of the μ_c/μ_b ratio⁴⁷.

In order to reproduce the FIR spectrum close to the estimated experimental accuracy up to $J \approx 55$, see Table II, we developed the rotational Hamiltonian H_{rot} to degree 8 in (J, K) , see Table I. We can see from Fig. 7, that this set of parameters was sufficient to randomize discrepancies. It also shows that these discrepancies grow very rapidly after $J = 50$, which may indicate an onset of a general perturbation by another state. Figure 9 shows that we have been able to reach practically all levels within the assigned J -multiplets, and in particular type- A levels at the high energy end. Note that in the scale of Fig. 9, the rotational structure of $|\nu_{11} = 1\rangle$ is indistinguishable from that of $|0\rangle$. The list of all assigned $0 \rightarrow \nu_{11}$ transitions is provided in supplementary materials to this paper²⁴.

There are a few problems that we encountered in the analysis of $0 \rightarrow \nu_{11}$. We should mention that the dense Q -branch extends far enough to obscure the low- J ${}^Q P$

TABLE II. Summary of the analysis of the spectroscopic data for DMSO used in our work: For each band, we give the total number $\mathcal{N}_{\text{total}}$ of assigned lines, the values of the total angular momentum J , the estimated unweighted σ_{u} and weighted σ_{w} standard errors of the fit, and the number of assigned lines $\mathcal{N}_{>2\sigma}$ with errors above $\pm 2\sigma$

Band	Frequencies	$\mathcal{N}_{\text{total}}$	J	$\mathcal{N}_{>2\sigma}$	2σ	σ_{u}	σ_{w}	Units
$0 \leftarrow \nu_{23}$	FIR	302–349 cm^{-1}	7608	4–60	526	10	5.081	10^{-4}cm^{-1}
$0 \leftarrow 0$	MW	6–702 GHz	3758	0–60	509	0.1	0.081	MHz
$0 \leftarrow \nu_{11}$	FIR	352–403 cm^{-1}	4577	5–56	369	10	5.603	10^{-4}cm^{-1}

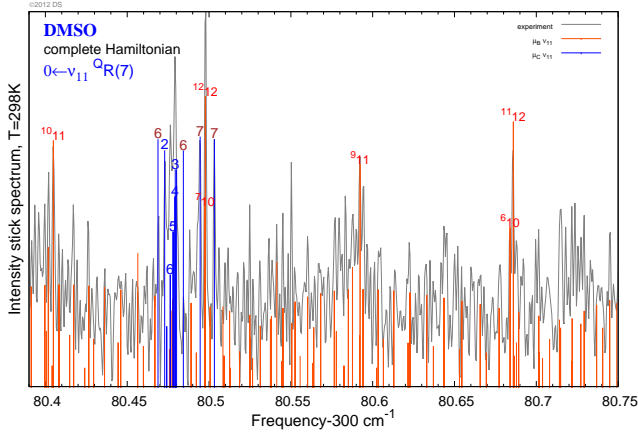


FIG. 6. The μ_c multiplet ${}^Q R(7)$ and the neighboring μ_b transitions ${}^R R(J)$ with $J = 10 \dots 12$ and $K_c = J, J-1, \dots$ in the $0 \rightarrow \nu_{11}$ spectrum. The observed FT-FIR spectrum is shown by gray solid line; blue and orange sticks mark computed intensities for dipole moments μ_c (\parallel component) and μ_b (\perp component). For the ${}^Q R(7)$ lines, their K_c or K_a assignments are displayed on top of the blue sticks in blue or brown, respectively; for the ${}^R R(J)$ lines, the $K_c J$ assignments are given in red on top of the orange sticks.

multiplets, while the ${}^Q R$ branch beginning is buried under additional dense bandheads, likely hot bands, off the high frequency head of the ${}^Q Q$ -branch. A number of relatively weak and sparse lines that did not belong to the ν_{11} band were probably of the same origin. We have also observed a persistent strong local perturbation of a single C -type level with $K_c \approx 15 \dots 16$ in multiplets with $J \approx 30 \dots 40$ (see gaps and dashed line in Fig. 9). Note that the perturbation cannot be ascribed to ν_{23} because the perturbed levels lie above the ν_{23} multiplet. One of the likely candidates for the dark perturber state is the $2\nu_{24}$ overtone of the antisymmetric methyl rocking vibration: According to our GAUSSIAN²⁷ computation, the harmonic frequency of ν_{24} is about 190 cm^{-1} and $2\nu_{24}$ should lie close to ν_{11} and should interact strongly with ν_{11} via a cubic Fermi term $a_{11}^+ a_{23}^2$. On the contrary, the symmetric $2\nu_{24}$ cannot interact with the antisymmetric ν_{23} through the same low order mechanism. In our isolated fit of ν_{11} , we excluded all strongly perturbed levels, but we retained some of their neighbors despite their characteristically diverging systematic errors as they approached the perturber, see Fig. 8. This may have in-

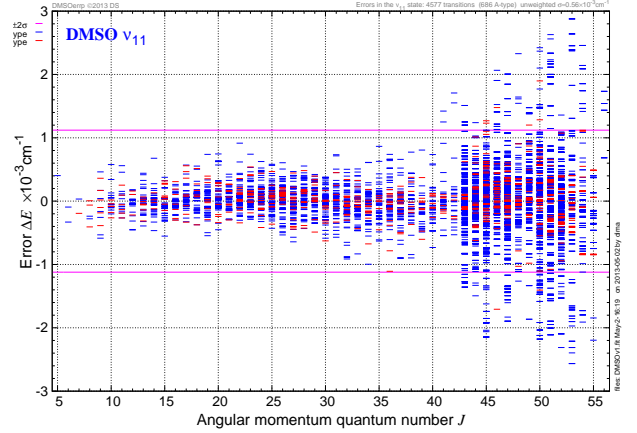


FIG. 7. Errors (theory–experiment) in reproducing rotational transitions in the ν_{11} FIR band. Color version: red and blue represent A and C -type levels, respectively.

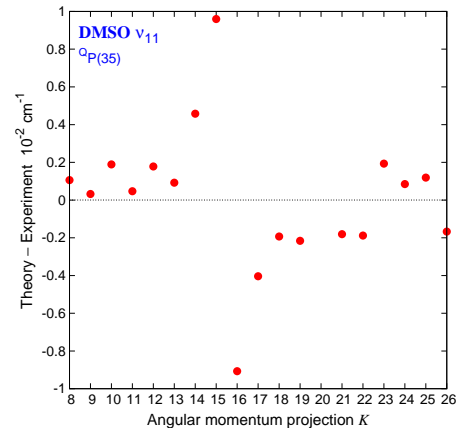


FIG. 8. Errors (theory–experiment) in reproducing rotational transitions in the ${}^Q P(35)$ sub-branch of $0 \rightarrow \nu_{11}$ exhibiting a local perturbation of ν_{11} near $K = 15-16$ for $J = 34$

creased slightly the overall unweighted error.

2. The ν_{23} fundamental transition

In comparison to $0 \rightarrow \nu_{11}$, the \perp -like $0 \rightarrow \nu_{23}$ spectrum is dense and complex. Unlike the ${}^Q R_{\approx J}(J)$ transitions of $0 \rightarrow \nu_{11}$, there is no line groups or regular sequences of lines that are directly identifiable from a

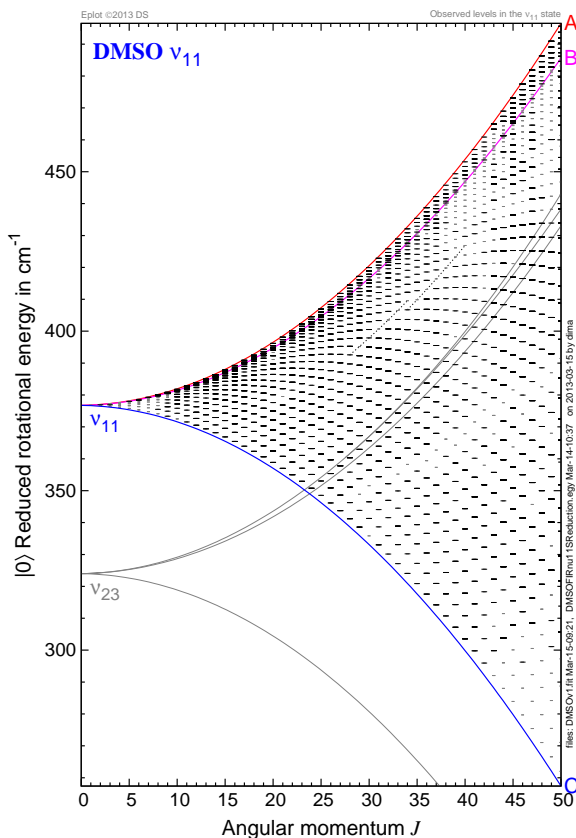


FIG. 9. Rotational structure of the vibrational state ν_{11} of DMSO reconstructed using parameters in Table I. Energies (level dashes) are shown after subtracting the average classical ground state rotational energy $(\mathcal{H}_{\text{rot}}^A(J) + \mathcal{H}_{\text{rot}}^C(J))/2$; observed levels are marked by longer dashes; bold solid lines represent energies of classical stationary axes of rotation (relative equilibria), the neighboring state ν_{23} is indicated in gray. A dashed line marks locally perturbed ν_{11} levels with $K = 15-16$ and $J = 30 \dots 40$.

simple model. The key to the assignment of $0 \rightarrow \nu_{23}$ is in the relatively weak reciprocal ${}^R Q_{K-1}$ and ${}^P Q_{K+1}$ sub-branches, the only regular features which are well visible in the central part of the spectrum (see Fig. 10(a) and Appendix²⁴ B 2) off the main Q -branch. Each sub-branch is a regular, compact series of lines with the same (K'_c, K''_c) and different $J = J' = J'' \geq \max(K'_c, K''_c)$, see Fig. 11. In this section, we denote the upper state (ν_{23}) quantum number K'_c as K . Then the lower state ($|0\rangle$) quantum number is $K-1$ and $K+1$ for ${}^R Q$ and ${}^P Q$, respectively. Because these sub-branches are nearly featureless sequences of lines, the assignment only by matching the frequency difference of the reciprocal ${}^R Q_{K-1}(J)$ and ${}^P Q_{K+1}(J)$ lines, sharing the same upper rotational level of ν_{23} , to the energy difference of the ground states $|J, K-1\rangle$ and $|J, K+1\rangle$, which is known very accurately. This technique is commonly used in spectroscopy.

In the simplest approximation for a rigid nearly sym-

metric top, averaging the small asymmetry term $(A-B)J_a^2$ over one period of the (fast) rotation about symmetric top axis (C), the rotational energy is written as

$$H_0(J, K) = B\mathbf{J}^2 + (C-B)K^2 + \frac{A-B}{2}(\mathbf{J}^2 - K^2).$$

Then the frequencies of ${}^R Q_{K-1}$ and ${}^P Q_{K+1}$ of transitions between levels with smallest $J \approx K$ are given approximately as $\omega_{23} + f_R^0(K)$ and $\omega_{23} + f_P^0(K)$, where

$$\begin{aligned} f_R^0(K) &= H_0(K, K) - H_0(K, K-1) \\ &= (C - \tilde{B})(2K - 1) \\ f_P^0(K) &= H_0(K+1, K) - H_0(K+1, K+1) \\ &= (\tilde{B} - C)(2K + 1), \end{aligned}$$

with $\tilde{B} = (A+B)/2$. Consequently, the rough estimate for the frequency difference between the reciprocal sub-branches is $4(\tilde{B} - C)K$. Picking the frequencies in the experimental spectrum as illustrated in Fig. 10(a), we can easily verify that the sequence is indeed quasi-linear in K . At this point, we can assign tentatively the reciprocal sub-branches sharing the same upper state with quantum number K . However, because the band centers are defined with considerable errors, the sub-branches with $K < 7$ are missing (the symmetric top approximation is too crude for small K), and the band origin is obscured, these K assignments are not error prone and several combinations of the K values have to be considered.

Finding the values of J is even more difficult because the sub-branch heads are not well pronounced, especially for ${}^P Q$, cf Fig. 11. Below we explain how our (J, K) assignments of the experimental frequencies $F_R(J, K)^{\text{exp}}$ and $F_P(J, K)^{\text{exp}}$ of spectral lines in the respective sub-branches were tested and confirmed. At first, plotting the reduced experimental frequencies

$$\tilde{F}_{P,R}^{\text{exp}}(J, K) := F_{P,R}^{\text{exp}}(J, K) - \omega_{23} - f_{P,R}^0(K)$$

versus K (Fig. 10(b)), gives a Loomis-Wood style diagram, which allows to follow continuous families in (J, K) across the sub-branches and to weed out all irrelevant lines. For each fixed K , we can approximate the series of frequencies $\tilde{F}_{P,R}^{\text{exp}}(J, K)$ using smooth polynomials $f_P^{\text{exp}}(J, K)$ and $f_R^{\text{exp}}(J, K)$. This works well for sufficiently large K , i.e., for C -type doublets, whose splittings are small compared to the experimental resolution. In our case, it worked for all $K \geq J/4$. Similarly, for the predicted frequencies $F_{P,R}(J, K)$, we obtain $\tilde{F}_{P,R}(J, K)$ and the respective polynomials $f_P(J, K)$ and $f_R(J, K)$. It can be seen that subtracting the quantity

$$f(J, K) = \frac{1}{2} [f_P(J, K) + f_R(J, K)]$$

from both $f_P(J, K)$ and $f_R(J, K)$ removes most of the dependence on the upper state. So if (J, K) are assigned correctly in both sub-branches, then

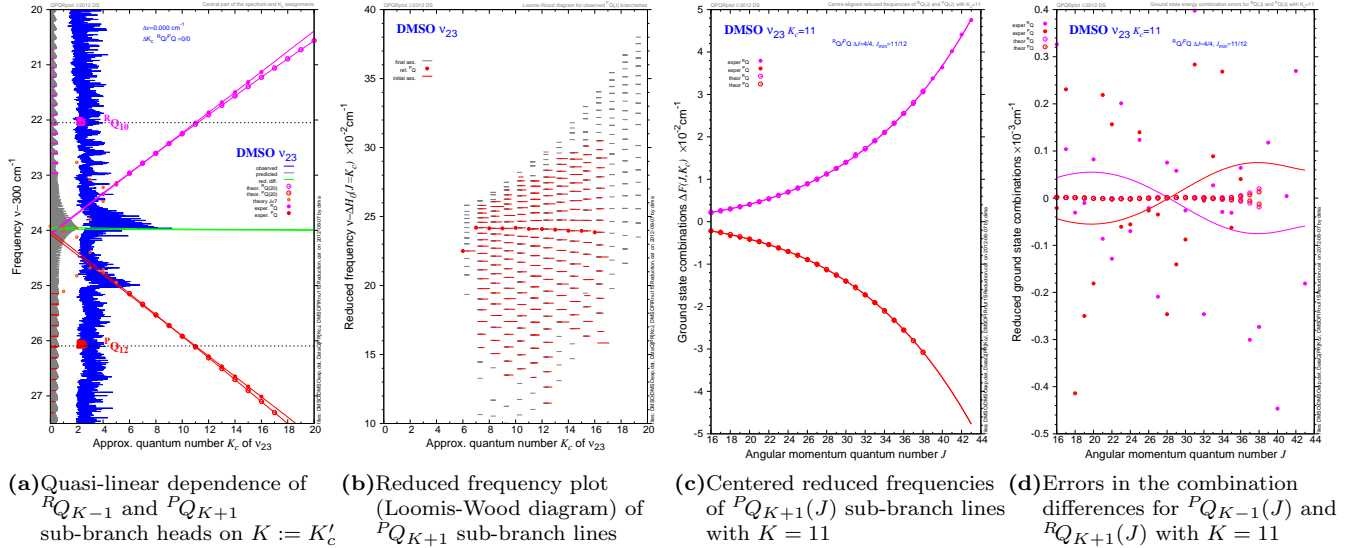


FIG. 10. Assignment of the reciprocal RQ_{K-1} and PQ_{K+1} sub-branches in the $0 \rightarrow \nu_{23}$ spectrum, see Sec. III E 2.

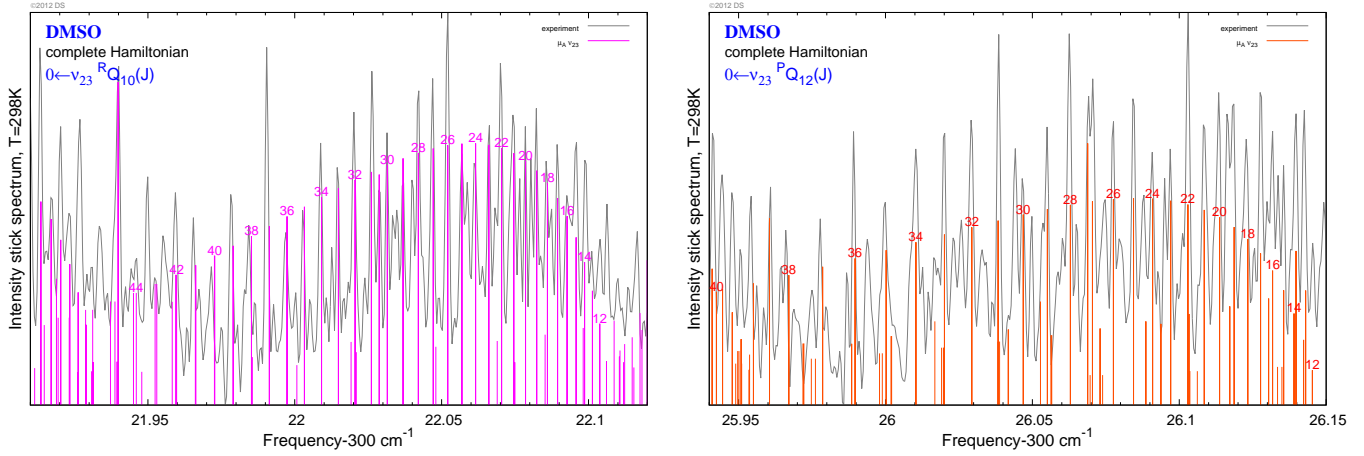


FIG. 11. Reciprocal multiplets $RQ_{10}(J)$ and $PQ_{12}(J)$ with $K = 11$ in the $0 \rightarrow \nu_{23}$ spectrum, cf Fig. 10(a). Gray line shows the observed FT-FIR spectrum; sticks mark computed intensities for the dipole moment μ_a (\perp component); J assignments are displayed on top of the sticks.

not only the differences $F_P^{\text{exp}}(J, K) - F_R^{\text{exp}}(J, K)$ and $f_P^{\text{exp}}(J, K) - f_R^{\text{exp}}(J, K)$ but also $f_P^{\text{exp}}(J, K) - f^{\text{exp}}(J, K)$ and $f_R^{\text{exp}}(J, K) - f^{\text{exp}}(J, K)$ become functions of the ground state energies only, and they should, therefore, coincide with the predicted $f_P(J, K) - f(J, K)$ and $f_R(J, K) - f(J, K)$ regardless how crude the upper state model is. This provides a quick test for the validity of the (J, K) sequence assignments.

We illustrate in Fig. 10(c) how this worked for $K = 11$. It can be seen that the family $f_P^{\text{exp}}(J, 11) - f^{\text{exp}}(J, 11)$ spans 0.05 cm^{-1} and, that at this scale, the agreement with the theory is perfect. As shown in Fig. 10(d), the errors can be visualized by plotting

$$\tilde{F}_s^{\text{exp}}(J, K) - f^{\text{exp}}(J, K) - (f_s(J, K) - f(J, K))$$

with $s = P, R$. We can see that the errors for the experimental frequencies are well randomized and are running into 10^{-3} cm^{-1} . Plotting the computed quantities

$$\tilde{F}_P(J, K) - f_P(J, K) \text{ and } \tilde{F}_R(J, K) - f_R(J, K)$$

at the same scale, we can also verify that the splittings become visible at $J \approx 40$ and remain well below the experimental errors.

Once a number of the RQ_{K-1} and PQ_{K+1} sub-branch pairs of $0 \rightarrow \nu_{23}$ was successfully found and assigned as described above, and the parameters of H_{rot} were fitted to reproduce the assigned lines and to generate sufficiently accurate, to about 0.005 cm^{-1} , predictions of the spectrum, advancing to larger J relied on a computerized procedure `acmbdif`. This procedure exploited

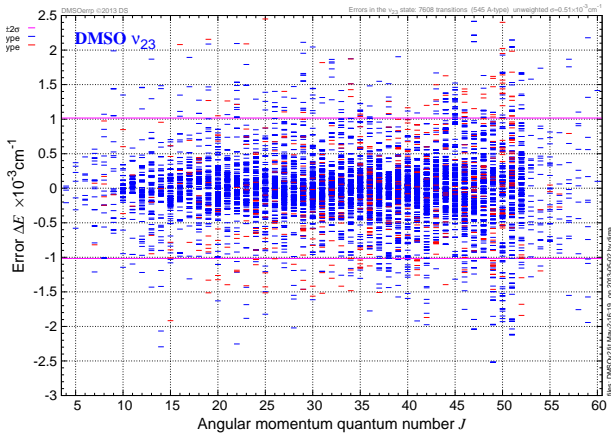


FIG. 12. Errors (theory–experiment) in reproducing rotational transitions in the ν_{23} FIR band. Color version: red and blue represent A and C-type levels, respectively.

systematically the ground state combination differences. Taking the ensemble of all predicted transitions to a given rotational state of ν_{23} , `acmbdif` allowed the ensemble as a whole to wiggle in absolute frequency position within, typically, an interval of 0.01 cm^{-1} near the prediction. A correlation function of the shifted ensemble against the experimental spectrum pointed to the best match(es). The response listing of `acmbdif` was analyzed in a specially configured editor, and the list of definite assignments was augmented and refitted. At the end, we were able to progress up until $J \approx 60$, while keeping the observed–calculated discrepancy well randomized and bracketed within $\pm 10^{-3} \text{ cm}^{-1}$, see Fig. 12. Normally, transitions, that were picked up by `acmbdif`, had to be checked further in order to weed out weak and/or blended lines. However, with the total number of $\nu_{23} \leftarrow 0$ assignments²⁴ growing above 7500, see Table II, this became physically impossible. This may explain why our mean square deviation of $5 \times 10^{-4} \text{ cm}^{-1}$ is slightly above the estimated experimental accuracy of 1.5×10^{-4} .

Like in the case of ν_{11} , the isolated state model reproduced adequately the ν_{23} data. We used an S -form rotational Hamiltonian $H_{\text{rot}}(\mathbf{J})$ with a complete set of phenomenological parameters to degree 8 in the components of \mathbf{J} , and with additional diagonal parameters of degree 10 in (J, K) , see Table I and Ref. 24. The most interesting immediate result of the analysis is the striking difference of the ν_{23} parameters from those of $|0\rangle$ and ν_{11} in Table I. Specifically, while the estimated parameter uncertainties were similar for both FIR bands, thus suggesting that correlations remained under control, the values of the parameters $d_{1,2}$ and $h_{1,2,3}$ of the respective S -form tensorial terms of degrees 4 and 6 were found much larger: at least $\times 20$ for $d_{1,2}$ and $\times 10^3$ for $h_{1,2,3}$.

Such difference in the parameter values is, undoubtedly, the consequence of the qualitatively different energy level structure of the ν_{23} rotational multiplet, see Fig. 13. The s -form tensorial terms contribute to low- K_c

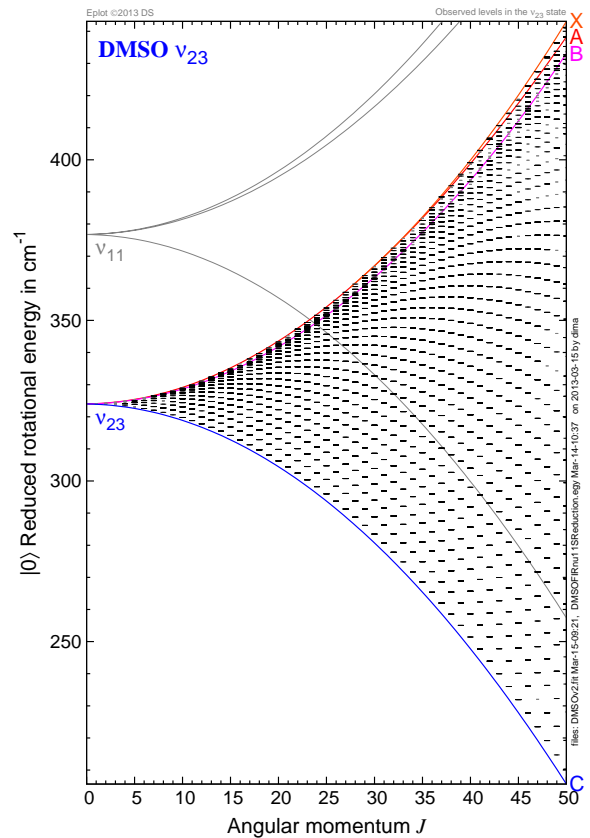


FIG. 13. Rotational structure of the vibrational state ν_{23} of DMSO reconstructed using parameters in Table I. Energies (horizontal dashes) are shown after subtracting the average classical ground state rotational energy $(\mathcal{H}_{\text{rot}}^A(J) + \mathcal{H}_{\text{rot}}^C(J))/2$; observed levels are marked by longer dashes; bold solid lines represent energies of classical stationary axes of rotation (relative equilibria), the neighboring state ν_{11} is indicated in gray.

states and the change of the structure should be anticipated near the energy $\mathcal{H}_{\text{rot}}^A$ of stationary rotation about axis A, i.e., at the high-energy end of the quantum multiplet in Fig. 13 and in the equatorial region of the classical \mathcal{H}_{rot} surface in Fig. 3(a). Indeed, we observe clearly that after $J = 35$, $\mathcal{H}_{\text{rot}}^A(J)$ is no longer the maximal energy, and there are quantum levels above it. It is also important to note that most of these high-energy X-type levels participate in the transitions that we were able to observe experimentally. Specifically, we have assigned 87 transitions involving 33 upper state levels of type X with $J = 37 \dots 57$ to 68 spectral lines listed in Table III. Thus we made sure that the structure of the high-energy end of the ν_{23} rotational multiplet was not just predicted from an extrapolation but was actually observed.

III. ROTATIONAL DYNAMICS

We can now give the classical dynamical interpretation of the rotational energy level structure of ν_{11} and ν_{23} in

TABLE III. Frequencies (cm^{-1}) and observed–calculated errors Err. (10^{-3} cm^{-1}) of the assigned lines in the far IR $\nu_{23} \leftarrow 0$ spectrum of DMSO, which involve the quadruple rotational states of type X of the fundamental vibrational excited state ν_{23}

Branch	$K'_a \leftarrow K''_a$	Frequency	Err.	Branch	$K'_a \leftarrow K''_a$	Frequency	Err.	Branch	$K'_a \leftarrow K''_a$	Frequency	Err.
$Q(37)$	$37 \leftarrow 37$	323.2623	-1.51	$Q(38)$	$38 \leftarrow 38$	323.1989	1.26	$Q(39)$	$39 \leftarrow 39$	323.1308	-0.24
$P(41)$	$40 \leftarrow 38$	308.1318	0.67	$Q(40)$	$40 \leftarrow 38$	325.9210	0.99	$Q(40)$	$40 \leftarrow 40$	323.0661	0.85
$P(42)$	$41 \leftarrow 39$	307.7111	-0.43	$Q(41)$	$41 \leftarrow 41$	323.0012	-0.53	$Q(41)$	$41 \leftarrow 39$	325.9328	-0.76
$Q(41)$	$41 \leftarrow 41$	323.0013	-0.48	$R(40)$	$41 \leftarrow 37$	346.2798	-1.12	$R(40)$	$41 \leftarrow 39$	343.6484	-1.26
$P(43)$	$41 \leftarrow 41$	305.5021	-0.14	$Q(42)$	$41 \leftarrow 39$	326.8646	-0.57	$Q(42)$	$42 \leftarrow 42$	322.9404	-1.87
$Q(42)$	$42 \leftarrow 40$	325.9506	0.60	$R(41)$	$41 \leftarrow 39$	345.0875	0.27	$R(41)$	$41 \leftarrow 41$	342.1558	0.46
$P(44)$	$43 \leftarrow 41$	306.9035	1.21	$Q(43)$	$43 \leftarrow 43$	322.8879	-0.77	$Q(43)$	$43 \leftarrow 43$	322.8879	-0.79
$R(42)$	$43 \leftarrow 41$	344.5408	-0.81	$Q(44)$	$43 \leftarrow 43$	324.1379	-1.40	$Q(45)$	$44 \leftarrow 42$	327.2196	0.41
$P(47)$	$45 \leftarrow 45$	303.9648	-0.40	$Q(46)$	$45 \leftarrow 43$	327.3496	-0.87	$Q(46)$	$45 \leftarrow 45$	324.2419	1.09
$Q(46)$	$46 \leftarrow 46$	322.7855	0.51	$R(45)$	$45 \leftarrow 43$	347.2680	-1.00	$P(48)$	$47 \leftarrow 47$	302.1282	0.61
$Q(47)$	$47 \leftarrow 45$	326.1600	-0.02	$Q(47)$	$47 \leftarrow 47$	322.7770	0.16	$R(46)$	$47 \leftarrow 45$	346.4350	-0.64
$Q(48)$	$47 \leftarrow 43$	330.4586	1.01	$Q(48)$	$47 \leftarrow 45$	327.6533	0.30	$Q(48)$	$48 \leftarrow 46$	326.2440	1.36
$R(47)$	$47 \leftarrow 45$	348.4195	-0.11	$R(47)$	$47 \leftarrow 47$	345.0373	0.93	$R(47)$	$48 \leftarrow 46$	346.9448	0.20
$Q(49)$	$48 \leftarrow 46$	327.8225	-0.33	$Q(49)$	$48 \leftarrow 46$	327.8225	-1.05	$Q(49)$	$49 \leftarrow 47$	326.3427	-0.75
$Q(49)$	$49 \leftarrow 49$	322.8110	-1.25	$R(48)$	$48 \leftarrow 48$	345.5573	-0.37	$R(48)$	$49 \leftarrow 47$	347.4712	-0.58
$Q(50)$	$49 \leftarrow 47$	328.0092	-0.31	$Q(50)$	$50 \leftarrow 48$	326.4638	-0.55	$Q(50)$	$50 \leftarrow 50$	322.8595	-0.06
$R(49)$	$49 \leftarrow 49$	346.0952	0.10	$R(49)$	$50 \leftarrow 48$	348.0185	-0.36	$P(52)$	$50 \leftarrow 46$	308.5613	1.32
$P(52)$	$50 \leftarrow 48$	305.6756	0.22	$Q(51)$	$49 \leftarrow 47$	326.6855	0.07	$Q(51)$	$50 \leftarrow 46$	331.2132	0.18
$Q(51)$	$50 \leftarrow 48$	328.2144	0.66	$Q(51)$	$50 \leftarrow 50$	324.7204	0.96	$Q(51)$	$51 \leftarrow 49$	326.6077	0.52
$R(50)$	$50 \leftarrow 50$	346.6513	0.87	$Q(52)$	$50 \leftarrow 44$	331.1607	-1.68	$Q(52)$	$50 \leftarrow 48$	326.6780	-1.00
$Q(52)$	$50 \leftarrow 50$	323.3191	-1.02	$Q(52)$	$50 \leftarrow 52$	319.5682	-0.97	$Q(54)$	$52 \leftarrow 54$	319.2692	-0.31
$Q(54)$	$52 \leftarrow 50$	326.6836	-1.20	$Q(55)$	$52 \leftarrow 54$	320.6033	-0.27	$Q(55)$	$54 \leftarrow 52$	329.2501	0.05
$Q(56)$	$54 \leftarrow 52$	326.7416	-0.27	$Q(56)$	$55 \leftarrow 53$	329.5756	-0.08	$Q(57)$	$57 \leftarrow 55$	328.0258	0.79

Figs. 9 and 13. Following the outline in Sec. IC, we convert our quantum rotational Hamiltonian H_{rot} into its classical analog \mathcal{H}_{rot} defined over the classical phase space \mathbb{S}_j^2 . For each given fixed value⁷ of j , $\mathcal{H}_{\text{rot}} : \mathbb{S}^2 \rightarrow \mathbb{R}$ can be represented conveniently as a deformed closed surface in the ambient space \mathbb{R}^3 . Specifically, points of this surface are given by

$$\mathbb{S}_j^2 \rightarrow \mathbb{R}^3 : (\theta, \phi) \mapsto \mathcal{H}_{\text{rot}}(\theta, \phi; j) \begin{pmatrix} \sin \theta \cos \phi \\ \sin \theta \sin \phi \\ \cos \theta \end{pmatrix}.$$

We draw such surfaces in Fig. 3 for the ground state $|0\rangle$ and for the excited state ν_{23} of DMSO, both with the same $J = 50$. Note that all classical mechanics computations in this section and Appendix²⁴ C rely on the standard calculus of functions $\mathbb{S}^2 \rightarrow \mathbb{R}$ representing rotational energy^{10,11,13,18,48}, such the ones illustrated in Fig. 3.

Subsequently, within the given interval $[0, 50]$ of j , we find all stationary points of \mathcal{H}_{rot} and determine their stability. In particular, for ν_{23} , we characterize the new stationary points X (Sec. IA, IIIA, Appendix²⁴ C2) and find the critical value j_{crit} at which they appear, i.e., the “moment of bifurcation”. The values of H_{rot} at the stationary points give the energies of classical stationary rotations, which we juxtapose on the quantum energy-momentum level diagrams in Figs. 9 and 13. The correspondence between the quantum rotational multiplets and these stationary values of H_{rot} as functions of j uncovers the nature of the changes observed in the level

structure.

A. Axes of stationary rotation

The six *fixed* points on \mathbb{S}_j^2 , representing axes²³ A , B , and C , and corresponding to Cartesian coordinate axes of the embedding \mathbb{R}^3 , are always stationary points⁸ of \mathcal{H}_{rot} . This can be seen as a direct consequence of the $D_2 \times \mathcal{T}$ symmetry²⁵ of \mathcal{H}_{rot} (Appendix²⁴ C1) and is independent on the concrete form of \mathcal{H}_{rot} . We can also see it from the calculation of $\nabla \mathcal{H}_{\text{rot}}$ in Appendix²⁴ C2.

As illustrated in Fig. 3, the \mathcal{H}_{rot} function of DMSO has deep minima on axis C (north and south poles) and small height variations along the equatorial ridge, i.e., for the C -projections $|j_c| \ll j$. In the symmetric top limit $A = B$, these ridge variations vanish, and \mathcal{H}_{rot} becomes the rotational energy function of an oblate top (a “pumpkin”). The C minima are so deep that nothing qualitative can happen to/near them with growing j . All nontrivial changes occur on/near the equatorial ridge.

B. Standard energy-angular momentum level system: the ground state and the ν_{11} state

In the ground vibrational state $|0\rangle$, see Fig. 3(b), and in the ν_{11} state, and in any state for sufficiently low j , the \mathcal{H}_{rot} function of DMSO is similar to that of a rigid oblate asymmetric Euler top: in addition to the two deep

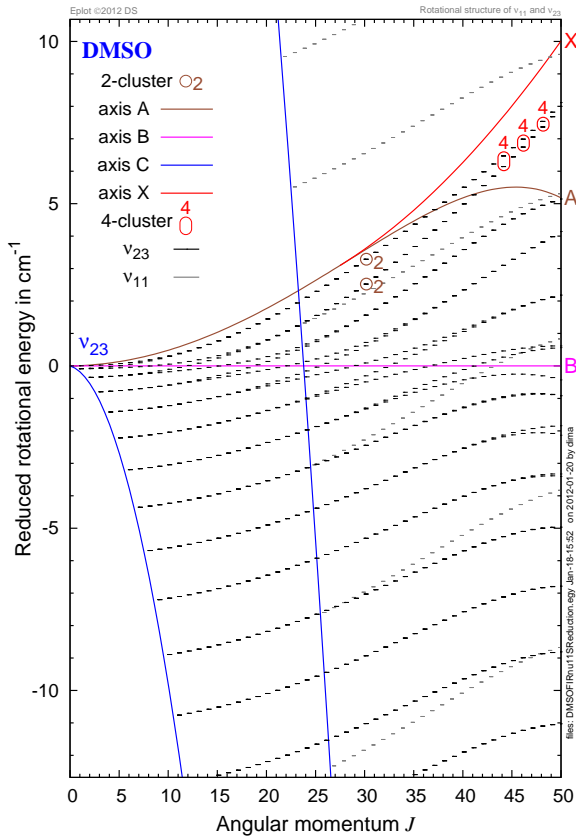


FIG. 14. Upper part of the rotational multiplet of the ν_{23} fundamental vibrational state of DMSO, cf Fig. 13. Energies are shown after subtracting the classical energy $\mathcal{H}_{\text{rot}}^B(J)$ of rotation about the unstable stationary axis B . Horizontal dashes mark quantum levels; bold solid lines represent energies of classical stationary rotations, the levels of the neighboring state ν_{11} are indicated in gray. Circles mark level sequences engaged in the X -type quadruplet formation. From Ref. 3

C -minima, it has two equivalent maxima A and two saddle points B . This means that rotations about A and C are stable and have, respectively, maximal and minimal energies $\mathcal{H}_{\text{rot}}^A(j)$ and $\mathcal{H}_{\text{rot}}^C(j)$ for a given j , while the rotation about B is unstable, and occurs at an intermediate energy close to $\mathcal{H}_{\text{rot}}^A(j)$.

The corresponding standard rotational structure of $|\nu_{11} = 1\rangle$ is shown in the energy–angular momentum diagram in Fig. 9 along with the stationary \mathcal{H}_{rot} values at A (maximum), B , and C (minimum). Quantum levels lie inside the energy–momentum domain bounded by $H_{\text{rot}}^A(j)$ and $H_{\text{rot}}^C(j)$. We see two sequences of doublets (or 2-clusters⁹): numerous C -doublets ascend from $H_{\text{rot}}^C(j)$, while a smaller number of A -doublets descend from $\mathcal{H}_{\text{rot}}^A(j)$. These sequences meet at $\mathcal{H}_{\text{rot}}^B(j)$, where the doublets split up and rearrange. The doublet quantum states with energies approaching $H_{\text{rot}}^S(j)$ with $\xi = A, C$ behave similarly to those of a one-dimensional two-well harmonic oscillator^{8,49}, whose frequency ω_ξ can be estimated from the distance in energy between the two dou-

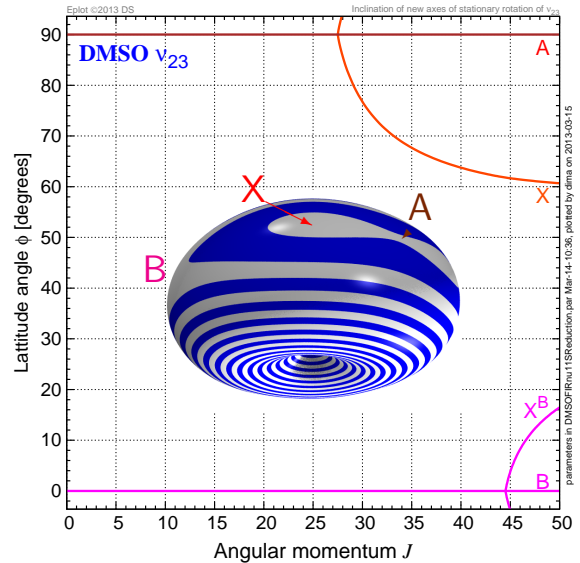


FIG. 15. Latitudinal tilt φ (degrees) of new axes X of stationary rotation in the ν_{23} state of DMSO, cf Fig. 3(a).

blet states closest to the classical value $H_{\text{rot}}^S(j)$. The outermost doublet is the most classically behaving and the most strongly degenerate state⁹; its distance to $\mathcal{H}_{\text{rot}}^S$ is about $\omega_\xi/2$. The stability of the classical equilibrium ξ is proportional to ω_ξ , notably $\omega_C \gg \omega_A$. Furthermore, the A well becomes deep enough to accommodate a quantum state only for $j \approx 10$, and the A -type doublets exist for $j \geq 10$. Our study (Ref. 2, Table I and Fig. 9 of this work) shows that, just like in the ground state $|0\rangle$, no qualitative complications due to the closeness of the symmetric top limit occur in the ν_{11} state when j increases. One may speculate that the two bulky methyl groups prohibit the decrease of the CSC angle when the molecule rotates about axis A .

C. Energy–angular momentum level system of ν_{23}

For low $j < 30$, the \mathcal{H}_{rot} function of the fundamental excited vibrational state ν_{23} (see Fig. 13) is qualitatively similar to that of $|0\rangle$ and ν_{11} described in Sec. III B above. At larger j , the equatorial ridge changes *qualitatively*, see Fig. 3(a) and Sec. I A. Here *both* principal axes A and B are unstable (saddle points), while near A on the ridge, we see a pair of new equivalent maxima X . These maxima emerge from A at $J_{\text{crit}} \approx 30$ after a pitchfork bifurcation. They correspond to a pair of new stationary rotation axes that lie in the equatorial plane AB at some angle to axis A . So altogether we have *four* equivalent corresponding points X on \mathbb{S}_j^2 and the corresponding four quantum levels. In Fig. 14, we can see that the energy $\mathcal{H}_{\text{rot}}^A(J)$ of classical rotation about the fixed stationary axis A is no longer maximal for $J > 30$. In fact, the two upmost J -sequences of the A -type doublets cross

above $\mathcal{H}_{\text{rot}}^A(J)$ into the X -domain and merge together thus forming a quadruplet or 4-cluster. We succeeded to identify a number of direct absorption transitions to these quadruplets (Table III).

1. The energy of classical rotation about the X axis

The isotropy group of the A point is an order 4 group isomorphic to $Z_2 \times Z_2$ (Appendix²⁴ C1). It is generated by C_2^A (rotation by π about A) and the reversal operation $\mathcal{T}C_2^C$, which amounts to a reflection of \mathbb{S}_j^2 in the equatorial plane AB , while its third nontrivial element $\mathcal{T}C_2^B$ acts as a reflection in the plane AC . Since in a one-parameter pitchfork bifurcation at A , only one of the order-2 symmetries of A can, typically, be broken, we can expect the pair of the new stationary points X to remain in either of the two symmetry planes. Given that at low j , the A -maximum is significantly less stable in the direction of the B -saddle than in the direction of the deep C -minimum, we may expect to find X in the equatorial plane AC . This is indeed the case (Appendix²⁴ C2). To find the position of X on the equator (see Fig. 15), we look for zeroes $\varphi_X(j) \in (0, \pi/2)$ of $\nabla_\varphi \mathcal{H}_{\text{rot}}(\theta = \pi/2, \varphi; j)$ for different values of j . We show in Appendix²⁴ C2 that these zeroes are given approximately by

$$(\cos \varphi_X)^2 \approx \frac{A - B}{4j^2 8d_2} + \frac{4d_2 - d_1}{8d_2}.$$

The corresponding stationary value $\mathcal{H}_{\text{rot}}^X(j) = \mathcal{H}_{\text{rot}}(\theta = \pi/2, \varphi_X(j); j)$ gives the energy of the rotation about X . For a given fixed $j > j_{\text{crit}} \approx 30$, this energy is maximal, see Figs. 13 and 14.

2. The pitchfork bifurcation

Finding the critical value j_{crit} of the angular momentum at which the X points emerge from A is equally straightforward: we should simply solve $\varphi_X(j) = \pi/2$, i.e., we should determine when the nontrivial zero $\varphi_X(j)$ enters the interval of allowed values. Taking \mathcal{H}_{rot} to the lowest nontrivial order (see Appendix²⁴ C3), the critical value of the quantum number⁷ J is given by

$$J_{\text{crit}}^2 \approx \frac{1}{4} \frac{(A + \delta A) - (B + \delta B)}{(d_1 + \delta d_1) - 4(d_2 + \delta d_2)}$$

(We use J here in order to compare directly with the energy level diagram in Figs. 13 and 14.) For the ν_{23} parameters in Table I, we obtain $J_{\text{crit}}^A \approx 31.5$. A numerical solution taking all orders in H_{rot} into account results in $J_{\text{crit}} = 27.5$. Furthermore, with higher orders of H_{rot} taken into account, we can also find that the unstable axis B bifurcates as well at larger $J_{\text{crit}}^B = 44.5$. This bifurcation sends out a pair of unstable equilibria, while B turns stable. This phenomenon is governed by 6-th order terms in H_{rot} . In our angular momentum range

$J_{\text{crit}}^B \leq J \leq 55$ (cf Table III), axis B remains marginally stable and the corresponding structure in the phase space \mathbb{S}_j^2 near it is not large and deep enough to manifest itself in the quantum energy spectrum.

3. The physical nature of the 4-clusters of DMSO

Considering the physical origins of the phenomenon of the 4-cluster formation, one comes up with two limiting mechanisms, “rotational” and “vibrational”. The rotational mechanism was put forward by Pavlichenkov and Zhilinskiĭ^{10–12}, whose rigid bender model^{48,50} is summarized in Appendix²⁴ D. In this model, similarly to the Born–Oppenheimer approximation, vibration and rotation are assumed to be well separated, and explicit vibration-rotation interactions are neglected entirely. The nonrigid molecule responds to the centrifugal forces by adjusting “instantaneously” its average equilibrium geometry, as the rotational excitation increases. This may result, in particular, in the new axes of stationary rotation.

In a more general situation of strongly interacting excited vibrational states formed by two or more resonant vibrational normal modes, we should consider stationary rotations in combination with *nonlinear normal modes* or vibrational relative equilibria (see Refs. 51 and 52, and references therein). These latter are specific low-order vibrational periodic orbits, whose number and symmetry properties may differ from those of the normal modes. One of the most familiar examples is the pair of equivalent stable “local modes” bifurcating out of a symmetric normal mode in a 1:1 resonant two-mode system (e.g., H_2O , O_3 , CS_2). The stationary rotation associated with local modes would necessarily produce 4-clusters, one doublet per each local mode. Even more generally, mixing of the vibrational states can be provoked not only by purely vibrational interactions, as in the above example of local modes, but also by Coriolis and other higher order rotation-vibration interactions⁵³. If this happens, we may have changes in the nature and numbers of rotation-vibration nonlinear modes and, respectively, in the degeneracies of the corresponding eigenstate clusters. When different vibrational normal mode basis state contributions to the eigenfunctions run high, Jensen and Koziņ proposed to call such clusters vibrational^{54–56}.

In this work, we have a limited capacity to elucidate the nature of the X -type quadruplets of the ν_{23} state of DMSO, because our information on several “dark state” neighbors of ν_{23} is incomplete, and because we stay at the level of the phenomenological Hamiltonian H_{rot} , that describes vibrational states as isolated. Nevertheless, we think that these quadruplets are more likely to be of the “rotational” kind, because we do not see sufficiently strong rotation-vibration interactions which involve ν_{23} .

Below we detail the argument. We explore several directions: Observed or predicted vibrational frequencies of the dark states (Sec. III C3 a); Explicit account

TABLE IV. Comparison of experimental and estimated frequencies (cm^{-1}) of bending vibrational modes of DMSO; G-h and G-a refer to harmonic and anharmonic frequencies computed using GAUSSIAN03²⁷, see Appendix²⁴ A. The experimental frequencies of ν_{13} and ν_{24} are obtained from the intensities of the respective MW satellite bands relative to those in the $0 \leftarrow 0$ band⁵⁷; the ν_{12} frequency comes from the liquid state Raman spectrum³⁵.

Mode	Observed	Ref. 29	G-h	G-a
ν_{11}	376.751	388.7	369.9	371.7
ν_{23}	323.988	331.3	319.4	321
ν_{12}	308	306.5	283.6	277
ν_{13}	231	219.5	232.7	177.5
ν_{24}	207	201.9	190.3	147.3

for vibration-rotation interactions (Sec. III C 3 b); Level crossings or “narrow” resonances (Sec. III C 3 c); Rotational structure of all potential perturbers (Sec. III C 3 d).

a. Vibrational frequencies of dark states There are two kinds of candidates for possible strong perturbers of ν_{23} , namely the two other bending fundamental states ν_{11} and ν_{12} , both of symmetry A' , and the rocking mode combination state $\nu_{13} + \nu_{24}$ of symmetry A'' . Their principle interaction mechanism with ν_{23} is different: Coriolis interaction for the fundamental states, and Fermi (cubic) resonance for the overtone. In either case, the respective terms a^+aJ and a^+a^2 are of order 3, and, as our study of the explicit Coriolis interaction of ν_{11} and ν_{23} , and of the local perturbations in the structure of ν_{11} (see Sec. II E 1 and paragraphs III C 3 b and III C 3 c below) may suggest, the perturber should come within 10 cm^{-1} or less of ν_{23} for any significant effects. While Typke and Dakkouri²⁹ place the dark state ν_{12} at 306 cm^{-1} , our calculation (Table IV, Appendix²⁴ A) gives consistently a much lower frequency. Since the same calculation reproduces the frequencies of both ν_{11} and ν_{23} quite accurately, we may assume that ν_{12} is indeed situated below 290 cm^{-1} , and so causes no significant perturbations to ν_{23} . The GAUSSIAN data on the rocking mode overtones being too unreliable, the vibrational $\nu_{13} + \nu_{24}$ frequency remains largely unknown. The naive harmonic estimate of 423 cm^{-1} is, of course, too high, but in conjunction with the observed crossings of ν_{11} with a rocking mode overtone (Sec. II E 1), one may speculate that $\nu_{13} + \nu_{24}$ lies above ν_{11} and far from ν_{23} , see Sec. III C 3 c.

b. Rotation-vibration interactions From the formal, phenomenological point of view, the 4-cluster formation and gyroscopic destabilization of axis A occur in the structure of ν_{23} because the d_1 and d_2 effective rotational constants of ν_{23} are anomalously large in comparison to those of $|0\rangle$ or ν_{11} (Table I). Recall that $d_1 K^2(J_+^2 + J_-^2)$ and $d_2(J_+^4 + J_-^4)$ are the principal tensorial terms of H_{rot} , that describe the dynamical asymmetry of the top in addition its average geometrical asymmetry given by $(A - B)$. So one can suspect that such anomalously large d_1 and d_2 account effectively for a strong and “wide”

rotation-vibration perturbation by a close neighbor state. In this work, taking the advantage of knowing rotational levels of both ν_{11} and ν_{23} , we have shown explicitly in Sec. II E 1, that the Coriolis interaction between these two states is insignificant, that the two states do not mix, and that in general, for such interaction to be important, the vibrational frequencies of the two states should be much closer, probably, of the order of 10 cm^{-1} or less.

c. Crossings with dark states A crossing with a dark state cannot distort the rotational constants significantly, unless the vibrational frequencies of the two states are close (so that the “crossing angle” is small), and the interaction is of relatively low order, i.e., we have a “large” resonance. This is why we are most interested in the Fermi resonance with doubly excited rocking modes. By symmetry, only $\nu_{24} + \nu_{13}$ can be in such resonance with ν_{23} , while the A' -type overtones $2\nu_{24}$ and $2\nu_{13}$ can Fermi interact with symmetric fundamentals ν_{11} and ν_{12} . Assuming that the crossings, that we observed in ν_{11} , are with the lowest double rocking mode excitation $2\nu_{24}$, we may exclude $\nu_{24} + \nu_{13}$, whose frequency is larger than that of $2\nu_{24}$, from the list of the perturber candidates. Yet more studies are clearly needed here. Thus most recently⁵⁸, pure rotational transitions in the 5 lowest frequency modes of DMSO have been measured using the new versatile subTHz spectrometer⁵⁹. This study provides a full set of the rotational parameters of the low frequency fundamental state and, possibly, of at least one perturber state candidate. However, the vibrational frequencies of these states remain unknown.

d. Rotational structure of neighbor states In general, if a strong and wide rotation-vibration mixing of ν_{23} with a neighbor state existed, the H_{rot} parameters of that potential perturber would also take anomalous values. Yet, according to our most recent observations⁵⁸ of the rotational spectra of excited vibrational states of DMSO, the other low energy fundamental states, most notably the inactive A' -type bending state ν_{12} , and also the two methyl rocking fundamentals ν_{13} and ν_{24} show no such anomaly. This definitely excludes ν_{12} . From the same observations⁵⁸, it should be possible to extract the information on the rotational structure of at least one more state, probably $2\nu_{24}$, the lowest of the double excited rocking states, and thus complete the argument.

4. Discussion of the physical mechanism

If not the vibrational and/or rotational resonant mixing mechanism, what else can be at the origin of the gyroscopic destabilization phenomenon that we have observed? Turning to the original ideas of Pavlichenkov and Zhilinskiĭ^{12,48}, we recall that when the equilibrium geometry of the molecule is nearly critical, very small forces—provided, of course, that they go in the “right direction”—are required to produce qualitative changes. Specifically, this happens when the principle moments of inertia are very close to those of a symmetric top, and

the usual qualitative stability of the asymmetric top rotational dynamics vanishes. For the rotational energy surfaces in Fig. 3, the critical situation manifests itself as a near axial symmetry of these surfaces. So even a relatively small perturbation at the equator can result in qualitative changes.

In the case of the AB_2 molecules with heavy central atom^{12,14,15,17,48,50,54–56}, the critical configuration occurs when the bend angle approaches $\approx 90^\circ$ (Appendix²⁴ D), and these molecules exhibit a bifurcation in the ground vibrational state, which is very similar to the one we observe in ν_{23} . In our case, even in a four-atomic rigid bender model of DMSO, the deformation is given by *three* angles. Furthermore, we should include fully the ν_{23} vibrational degree of freedom, the only antisymmetric bending vibration of the C_2SO frame, into consideration. This particular vibration seems to be essential to the phenomenon. We can assume that it “softens” the C_2SO frame, and amplifies specific dynamical responses to the centrifugal forces associated with fast rotation about axis A . In other words, while in the ground vibrational state of AB_2 , the centrifugal forces alone drive the molecule through the critical configuration, in our case, these forces combine with vibrational excitation. It is possible that a classical rigid bender calculation with parameters imitating DMSO can elucidate the matter.

IV. CONCLUSION

During the last decade, a number of synchrotron facilities, notably the Canadian Light Source, the Australian synchrotron, SOLEIL⁴, and others, have provided different beamlines that can be used for high resolution spectroscopy^{60,61} and have thus provided a great number of new objects of detailed studies. Our analysis of the ν_{11} and ν_{23} bands of DMSO (Refs. 2 and 3 and this work) demonstrated most convincingly the potential of the synchrotron spectroscopy in the far IR. Presently, we made substantial progress in unraveling the rovibrational structure of low frequency bending and torsional vibrational states of DMSO. Important, comprehensive, previously inaccessible structural and spectroscopic information on this molecule was obtained.

DMSO, due to its exceptional near-symmetric-top geometry, is a molecule with potentially complex and interesting rotational dynamics. Using the FIR data on the ν_{23} state, we have succeeded to uncover such dynamics. The phenomenon of the gyroscopic destabilization of the principle axis of inertia A of DMSO is very similar to that predicted and found in the AB_2 molecules in the 1990s, albeit now we deal with a much larger and significantly more complex polyatomic system. DMSO is the first known large molecule presenting this universal phenomenon.

ACKNOWLEDGMENTS

We thank Professor B. I. Zhilinskiĭ for discussions. We are grateful to Doctors O. Pirali, P. Roy, and J. B. Brubach of the AILES group at SOLEIL for their help during experiments. This work was partially funded by the Délégation Générale pour l’Armement (projet de Recherche Exploratoire et Innovation n° 06.34.037).

-
- ¹A. Cuisset, I. Smirnova, R. Bocquet, F. Hindle, G. Mouret, C. Yang, O. Pirali, and P. Roy, A.I.P. Conf. Proc. **1214**, 85 (2010).
- ²A. Cuisset, L. Nanobashvili, I. Smirnova, R. Bocquet, F. Hindle, G. Mouret, O. Pirali, P. Roy, and D. A. Sadovskii, *Chem. Phys. Lett.* **492**, 30 (2010).
- ³A. Cuisset, O. Pirali, and D. A. Sadovskii, *Phys. Rev. Lett.* **109**, 094101 (2012).
- ⁴P. Roy, M. Rouzières, Z. Qi, and O. Chubar, *Infr. Phys. and Techn.* **49**, 139 (2006).
- ⁵J. B. Brubach, L. Manceron, M. Rouzières, O. Pirali, D. Balcon, F. K. Tchana, V. Boudon, M. Tudorie, T. Huet, A. Cuisset, and P. Roy, A.I.P. Conf. Proc. **1214**, 81 (2010).
- ⁶Thus, not substantially toxic itself, DMSO is considered to be a simulant of such toxic organosulfide agents as the mustard gas $(Cl-CH_2CH_2)_2S$ (*Yperite*), and monitoring its concentrations is of interest to civil protection. DMSO’s wide deployment as an industrial solvent also calls for stricter environmental controls and monitoring.
- ⁷We denote the classical angular momentum and the corresponding quantum operator as vectors $\mathbf{j} = (j_a, j_b, j_c)$ and $\mathbf{J} = (J_a, J_b, J_c)$ whose body-fixed components are defined with respect to the principal axes of inertia²³ (A, B, C). The length of \mathbf{j} is denoted $j := \|\mathbf{j}\|$. Scaling quantum angular momenta by \hbar so that $j = \hbar\|\mathbf{J}\|$, we have $\|\mathbf{J}\| = \sqrt{J(J+1)}$ with quantum number $J = 0, 1, 2, \dots$. Then the classical limit of $\hbar \rightarrow 0$ corresponds to $J \rightarrow \infty$.
- ⁸When the absolute value of the projection j_ξ of the angular momentum vector \mathbf{j} on a stable axis ξ is near its maximum $j := \|\mathbf{j}\|$, the body rotates so that \mathbf{j} *precesses* about ξ . On the reduced phase space \mathbb{S}_j^2 of the Euler top that represents all possible orientations of \mathbf{j} , the trajectory encircles the elliptic point ξ .
- ⁹Near any sufficiently stable axis ξ , rotational states localize similarly to the symmetric top eigenstates $|J, J_\xi\rangle$ with projection $J_\xi = \pm J$ (for the most localized states), $\pm(J-1)$, etc. Spectroscopists call $K_\xi = |J_\xi|$ and ξ *good quantum number* and *quantization axis*. Due to the reversal symmetry²⁵, localized states form nearly degenerate *doublets* with dominant contribution from $|J, \pm J_\xi\rangle$.
- ¹⁰I. M. Pavlichenkov and B. I. Zhilinskiĭ, *Chem. Phys.* **100**, 339 (1985).
- ¹¹I. M. Pavlichenkov and B. I. Zhilinskiĭ, *Ann. Phys. (N.Y.)* **184**, 1 (1988).
- ¹²I. M. Pavlichenkov, *Physics Reports* **226**, 173 (1993).
- ¹³W. G. Harter and C. W. Patterson, *J. Chem. Phys.* **80**, 4241 (1984).
- ¹⁴M. Y. Tretyakov, S. P. Belov, I. N. Kozin, and O. L. Polyansky, *J. Molec. Spectrosc.* **154**, 163 (1992).
- ¹⁵I. N. Kozin, S. P. Belov, O. L. Polyansky, and M. Y. Tretyakov, *J. Molec. Spectrosc.* **152**, 13 (1992); I. N. Kozin, S. Klee, P. Jensen, O. L. Polyansky, and I. M. Pavlichenkov, *J. Molec. Spectrosc.* **158**, 409 (1993).
- ¹⁶J.-M. Flaud, C. Camy-Peyret, H. Bürger, P. Jensen, and I. N. Kozin, *J. Molec. Spectrosc.* **172**, 194 (1995).
- ¹⁷I. N. Kozin, P. Jensen, O. Polanz, S. Klee, L. Poteau, and J. Demaison, *J. Molec. Spectrosc.* **180**, 402 (1996).
- ¹⁸Z. Li, L. Xiao, and M. E. Kellman, *J. Chem. Phys.* **92**, 2251

- (1990); L. Xiao and M. E. Kellman, *J. Chem. Phys.* **93**, 5805 (1990).
- ¹⁹M. E. Kellman and V. Tyng, *Phys. Rev. A* **66**, 013602 (2002).
- ²⁰R. Somma, G. Ortiz, H. Barnum, E. Knill, and L. Viola, *Phys. Rev. A* **70**, 042311 (2004); A. P. Hines, R. H. McKenzie, and G. J. Milburn, *Phys. Rev. A* **71**, 042303 (2005).
- ²¹R. Gilmore, S. Kais, and R. D. Levine, *Phys. Rev. A* **34**, 2442 (1986).
- ²²S. Aubry, S. Flach, K. Kladko, and E. Olbrich, *Phys. Rev. Lett.* **76**, 1607 (1996).
- ²³Our molecule-fixed coordinates use the principal axes of inertia labeled (A, B, C) ; the same letters stand for the *rotational constants* $A = (2I_A)^{-1}$, etc of the rigid body. By the convention used, in particular, by Pickett's programs^{43,44} for the oblate tops, the axes (A, B, C) correspond to the standard axes (y, x, z) .
- ²⁴See Supplementary Materials for a complete listing of the $0 \leftarrow 0$, $\nu_{11} \leftarrow 0$, and $\nu_{23} \leftarrow 0$ assigned transitions of DMSO, and the list of spectroscopic parameters (Table 1) in Pickett's `lin` and `par` file formats^{43,44}, respectively. Appendices and the animated rotational energy surface of the ν_{23} of DMSO with $30 \leq J \leq 60$ can be found in the respective supplementary material files `Appendices-Cuisset-Sadovskii-JCPA13020201.pdf` and `DMSOsRE-animj.gif`.
- ²⁵The momentum (or time) reversal invariance of H_{rot} reflects the independence of the classical free rotation energy on the direction of rotation. Rotations by π about the principal axes of inertia form a dihedral group D_2 ; reduction of H_{rot} to a D_2 symmetric form was given by Watson⁶².
- ²⁶Bifurcations in systems with excited resonant vibrations, notably H_2S and again H_2Se , or spherical tops, should be treated within a broader framework of *rovibrational relative equilibria*, i.e., vibrational nonlinear normal modes associated with particular axes of stationary rotation. Such approach covers the whole range of critical phenomena from axis reorientation in an isolated nondegenerate vibrational state¹⁰ to the formation of *local modes*¹⁸.
- ²⁷M. J. Frisch *et al.*, *Computer program GAUSSIAN 03*, Rev. D.01, Gaussian, Inc., Wallingford, CT (2004).
- ²⁸ C_s is a point group of order 2 whose elements are reflection plane σ and identity $1 = \sigma^2$; its two one-dimensional irreducible representations are commonly denoted as A' (symmetric) and A'' (asymmetric).
- ²⁹V. Typke and M. Dakkouri, *J. Molec. Struct.* **599**, 177 (2001), and references therein; V. Typke, *J. Molec. Spectrosc.* **63**, 170 (1976), see Table II on p. 174 for mw data on DMSO.
- ³⁰D. Papousek and M. R. Aliev, *Molecular vibrational-rotational spectra*, Studies in Phys. and Theor. Chem., Vol. 17 (Elsevier, Amsterdam, 1982) for asymmetric top molecules see Chap. III.17 on p. 160.
- ³¹V. Typke, *J. Molec. Struct.* **384**, 35 (1996).
- ³²B. I. Zhilinskiĭ, private communication (2010), DMSO is so close to the symmetric top that moments of inertia of its ^{18}O isotope are reversed $I_C > I_A \gtrsim I_B$ and both stable axes lie in the symmetry plane.
- ³³W. Feder, H. Dreizler, H. D. Rudolph, and V. Typke, *Z. Naturforsch. A* **24**, 266 (1969); E. Fliege, H. Dreizler, and V. Typke, *ibid.* **38**, 668 (1983).
- ³⁴L. Margulès, R. A. Motiyenko, E. A. Alekseev, and J. Demaison, *J. Molec. Spectrosc.* **260**, 23 (2010).
- ³⁵G. Geiseler and G. Hanschmann, *J. Molec. Struct.* **11**, 283 (1972).
- ³⁶A. R. W. McKellar, *J. Molec. Spectrosc.* **262**, 1 (2010).
- ³⁷F. Kwabia Tchana, J. M. Flaud, W. J. Lafferty, L. Manceron, and P. Roy, *J. Quant. Spectrosc. Rad. Transf.* **111**, 1277 (2010); O. Piralı, V. Boudon, J. Oomens, and M. Vervloet, *J. Chem. Phys.* **136**, 024310 (2012); S. Yu, J. C. Pearson, B. J. Drouin, K. Sung, O. Piralı, M. Vervloet, M.-A. Martin-Drumel, C. P. Endres, T. Shiraishi, K. Kobayashi, and F. Matsushima, *J. Chem. Phys.* **133**, 174317 (2010).
- ³⁸L. S. Rothman *et al.*, *J. Quant. Spectrosc. Rad. Transf.* **110**, 533 (2009).
- ³⁹J. K. G. Watson, in *Vibrational Spectra and Structure*, Vol. 6, edited by J. R. Durig (Elsevier, 1977) pp. 1–89.
- ⁴⁰M. R. Aliev and J. K. G. Watson, in *Molecular Spectroscopy - Modern Research*, Vol. III, edited by K. N. Rao (Academic Press, 1985) pp. 1–67.
- ⁴¹The vibrational part of terms in Eq. (2) is of symmetry type A'' and therefore, these terms include components J_b and J_c of the angular momentum vector which change sign under reflection in the symmetry plane of the molecule (cf Fig. 1).
- ⁴²Following the contemporary, standard spectroscopic notation, transitions with the upper state $|J'', K''\rangle$ and the lower state $|J', K'\rangle$ are denoted as $|J', K'\rangle \leftarrow |J'', K''\rangle$; a series with fixed $\Delta K_c = K'' - K'$ and $\Delta J = J'' - J'$ is called branch and is denoted $\Delta^K \Delta J$, e.g., ${}^P R$; a line in the branch is referred as $\Delta^K \Delta J_{K'}(J')$.
- ⁴³H. M. Pickett, *J. Molec. Spectrosc.* **148**, 371 (1991).
- ⁴⁴H. M. Pickett, "SPFIT/SPCAT programs for vibration-rotation spectra," (2007), for more information and examples see also <http://www.ph1.uni-koeln.de/cdms/pickett> and <http://info.ifpan.edu.pl/~kisiel/asym/pickett/crib.htm>.
- ⁴⁵Z. Kisiel, "ASCP/SVIEW programs for graphical assignments of vibration-rotation spectra," (2009), for applications see Ref. 46.
- ⁴⁶Z. Kisiel, L. Pyszczólkowski, I. R. Medvedev, M. Winnewisser, F. C. D. Lucia, and E. Herbst, *J. Molec. Spectrosc.* **233**, 231 (2005).
- ⁴⁷A qualitative fit of the transition moment was not attempted because the FIR experiment in Fig. 2 was not corrected for the base line and gain.
- ⁴⁸I. M. Pavlichenkov and B. I. Zhilinskiĭ, *Opt. Spectrosk. (USSR)* **64**, 413 (1988), translated from Russian; *Optika i Spectroscopia* **64**, 688 (1988), in Russian.
- ⁴⁹The equivalence between the states of the one-dimensional oscillator and those of a rotator near a stationary axis of rotation can be demonstrated using the Holstein-Primakoff boson map approximation⁶³.
- ⁵⁰I. N. Kozin and I. M. Pavlichenkov, *J. Chem. Phys.* **104**, 4105 (1996); I. Kozin and I. M. Pavlichenkov, *JETP* **85**, 673 (1997).
- ⁵¹K. Efstathiou, D. A. Sadovskii, and B. I. Zhilinskiĭ, *SIAM Journal on Applied Dynamical Systems (SIADS)* **3**, 261 (2004).
- ⁵²H. Croghan, V. Boudon, and D. A. Sadovskii, *Europ. Phys. J. D* **42**, 61 (2007).
- ⁵³K. K. Lehmann, *J. Chem. Phys.* **95**, 2361 (1991).
- ⁵⁴P. Jensen and I. N. Kozin, *J. Molec. Spectrosc.* **160**, 39 (1993).
- ⁵⁵I. N. Kozin and P. Jensen, *J. Molec. Spectrosc.* **161**, 186 (1993).
- ⁵⁶I. N. Kozin and P. Jensen, *J. Molec. Spectrosc.* **163**, 483 (1994).
- ⁵⁷H. Dreizler and G. Dendl, *Z. Naturforsch.* **20a**, 30 (1965); **20a**, 1431 (1965).
- ⁵⁸A. Cuisset, M. A. Martin Drumel, F. Hindle, G. Mouret, and D. A. Sadovskii, "Experimental high-resolution study of the rotational structure of bending and rocking fundamental vibrational states of dimethylsulfoxide," (2013), the new, more complete MW spectrum of DMSO is recorded using a versatile very sensitive subTHz spectrometer. Rotational constants and centrifugal distortion corrections to order 6 for all low frequency bending and methyl rocking fundamental vibrational states ν_{11} , ν_{23} , ν_{12} , and ν_{13} , ν_{24} , respectively, are obtained from the analysis of the spectrum. In preparation to be submitted.
- ⁵⁹G. Mouret, M. Guinet, A. Cuisset, L. Croize, S. Eliet, R. Bocquet, and F. Hindle, *IEEE Sensors Journal* **13**, 133 (2013).
- ⁶⁰A. R. W. McKellar and B. Billingham, *J. Molec. Spectrosc.* **260**, 66 (2010).
- ⁶¹T. Chimdi, E. G. Robertson, L. Puskar, C. D. Thompson, M. J. Tobin, and D. McNaughton, *Chem. Phys. Lett.* **465**, 203 (2008).
- ⁶²J. K. G. Watson, *J. Chem. Phys.* **46**, 1935 (1967).
- ⁶³T. Holstein and H. Primakoff, *Phys. Rev.* **58**, 1098 (1940).
- ⁶⁴C. T. Lee, W. T. Yang, and R. G. Parr, *Phys. Rev. B* **37**, 785 (1988).
- ⁶⁵W. Kohn, A. D. Becke, and R. G. Parr, *J. Phys. Chem.* **100**, 12974 (1996).
- ⁶⁶A. Cuisset, G. Mouret, O. Piralı, P. Roy, F. Cazier, H. Nouali, and J. Demaison, *J. Phys. Chem. B* **112**, 12516 (2008).
- ⁶⁷L. D. Landau and E. M. Lifshitz, *Quantum mechanics (nonrela-*

tivistic theory), 5th ed., Theoretical physics, Vol. III (Fizmatlit, Moscow, 2002) in Russian.

⁶⁸The minus sign in front of $d\boldsymbol{\mu}/d\theta$ is due to the fact that $\boldsymbol{\mu}$ and

S–O are antiparallel; it has no relation to the minus sign in front of μ_b^0/μ_c^0 .

⁶⁹L. Michel and B. I. Zhilinskiĭ, *Physics Reports* **341**, 11 (2001).

APPENDICES OF JCP A13.02.0201

The manuscript A13.02.0201 entitled “Gyroscopic destabilisation in polyatomic molecules. Rotational structure of the low-frequency bending vibrational states ν_{23} and ν_{11} of dimethylsulfoxide” by Arnaud Cuisset and Dmitrii A. Sadovskii was submitted to *J. Chem. Phys.* on 2013-02-20, and on 2013-05-02 in final form.

Following the referees’ and editors’ suggestions, these appendices are moved to the file `Appendices-Cuisset-Sadovskii-JCPA13020201.pdf` in the supplementary materials (EPAPS), which is available to readers via an url link in the online version of the paper. They can also be obtained by contacting `arnaud.cuisset@univ-littoral.fr`. Note that all citations below use the bibliography in the main body of the paper.

Appendix A: Frequencies of bending vibrations of DMSO

All calculations were performed with GAUSSIAN03²⁷. To make a compromise between the overall cost and the accuracy of frequency calculations, the semi-empirical density functional theory (DFT) using the Becke three parameter hybrid exchange functional and the Lee-Yang-Parr correlation functional (B3LYP)^{64,65} was chosen for the DMSO structure optimizations and vibrational frequency calculations. The optimizations used the TIGHT and GDIIIS convergence criteria, which ensured the adequate convergence and the reliability of the computed frequencies, especially for low-frequency modes. In comparison to the experimental far IR (FIR) vibrational frequencies, the best results were obtained using the 6-311G++(3df,2p) basis. With such relatively large basis set, it was still possible to compute the anharmonic force field of DMSO, and to determine the rotational constants of the vibrationally excited states, as well as the frequencies of the combination bands and overtones. Table IV presents computed and measured FIR frequencies. With relative uncertainties better than 2%, the agreement is excellent between the fitted band centers of ν_{11} and ν_{23} and the DFT anharmonic calculations. For the lowest frequency modes ν_{12} , ν_{13} and ν_{24} , which were not observed in the FIR spectrum, the harmonic calculations agree better⁶⁶ both with the force field by Typke and Dakkouri²⁹ and the experimental frequencies from previous microwave and Raman spectroscopic studies³³.

Appendix B: Qualitative understanding of intensities

The “accidental” near symmetric top geometry of the equilibrium configuration of DMSO (Fig. 1) may call for the use of the symmetric top analogy in describing its rotation-vibration absorption spectra. Here we discuss the substantial difference between the DMSO spectra and those of a “true” symmetric top—a molecule for which

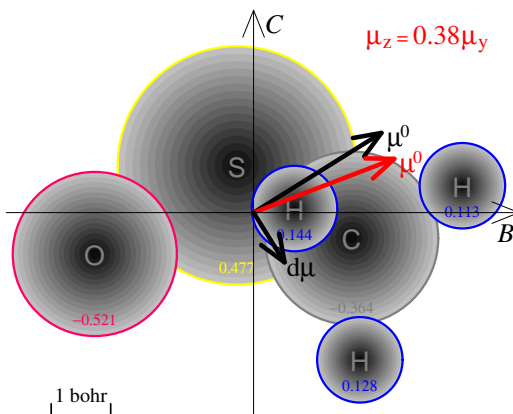


FIG. 16. Equilibrium configuration of DMSO (cf Fig. 1) projected in the the symmetry plane BC ; bold arrows show permanent dipole moment μ^0 and dipole moment $d\mu$ induced by the in-plane pendular motion of $S-O$. The rough estimate for μ^0 is aligned with $S-O$, and is shown in black. A more realistic dipole moment μ^0 , which is obtained by taking into account effective charge of each atom, is shown in red; effective charges and atom positions are computed using GAUSSIAN²⁷.

the equality of the two moments of inertia $I_A = I_B$ is caused by a sufficiently high symmetry of its equilibrium configuration. (For the description of the symmetric top selection rules see, for example, Ref. 30, Appendix J and Ref. 67, Chapt. XIV-110.)

1. The dipole moment function and its parameters

The dipole moment vector function of DMSO $\mu(q)$ is at the root of all differences: unlike the equilibrium geometry, $\mu(q)$ is very far from that of a symmetric top molecule. In the simplest approximation that is sufficient to describe the $0 \rightarrow 0$ rotational spectrum and the $0 \rightarrow 1$ fundamental transitions, the body-fixed²³ components of $\mu(q)$ can be represented as a Taylor series

$$\mu(q) = \begin{pmatrix} \mu_a \\ \mu_b \\ \mu_c \end{pmatrix} = \begin{pmatrix} 0 \\ \mu_b^0 \\ \mu_c^0 \end{pmatrix} + \begin{pmatrix} \mu_a^{23} q_{23} \\ \mu_b^{11} q_{11} \\ \mu_c^{11} q_{11} \end{pmatrix} + \dots$$

in normal displacements q . This differs from a true symmetric top molecule, which has axial symmetry $C_n \subset SO(2)$ with $n \geq 3$, or higher. In a true symmetric top, μ_c^0 is the only permanent component of μ , a “parallel” vibration cannot contribute neither to μ_b nor to μ_a , while a “perpendicular” vibrational mode is degenerate and contributes both to μ_a and μ_b .

The parameters of $\mu(q)$ (coefficients of the series) for DMSO can be roughly estimated by taking into account that atoms O and S of this molecule are highly polarized, while the combined charge on the methyls is nearly zero.

Then computing the permanent dipole moment

$$\boldsymbol{\mu}^0 \approx (\mathbf{r}_S - \mathbf{r}_O) \delta$$

for the equilibrium configuration in Fig. 1 and 16 and a charge $\delta > 0$ on atom S gives ($\text{\AA} \cdot \text{C}$)

$$\mu_b^0 \approx 1.264\delta \quad \text{and} \quad \mu_c^0 \approx 0.788\delta = 0.623\mu_b^0.$$

As illustrated in Fig. 16, this permanent dipole moment lies in the symmetry plane BC and is parallel to the S–O bond; the ratio μ_b^0/μ_c^0 is given by the tangent of the angle θ between S–O and axis C (vertical). A more precise estimate for $\boldsymbol{\mu}^0$ can be given using GAUSSIAN²⁷ predictions of both equilibrium positions and effective charges on each atom.

$$\mu_c^0 = 0.38\mu_b^0.$$

The same approach allows to estimate the ratio of the two components of the dipole moment $\boldsymbol{\mu}^{11}$ induced by the symmetric bending vibration ν_{11} . Indeed, assuming that such vibration causes in-plane pendular motion of S–O about its equilibrium position, while the distance S–O remains nearly unchanged, we obtain the induced dipole moment $\boldsymbol{\mu}^{11}$ as axial angle derivative⁶⁸

$$(-d\boldsymbol{\mu}/d\theta)d\theta = \|\boldsymbol{\mu}^0\| \begin{pmatrix} 0 \\ -\cos\theta \\ \sin\theta \end{pmatrix} d\theta$$

and therefore (cf Fig. 16)

$$\mu_c^{11}/\mu_b^{11} \approx -\mu_b^0/\mu_c^0.$$

So it follows that, with all other factors equal, the non-symmetric-top transitions in the rotational $0 \rightarrow 0$ spectrum of DMSO should be about $(\mu_b^0/\mu_c^0)^2$ stronger. Indeed, from our recent microwave measurements⁵⁸, we deduced $\mu_c^0/\mu_b^0 \approx 0.33$, which agrees well with the GAUSSIAN prediction. On the other hand, such transitions in $0 \rightarrow \nu_{11}$ are weakened by the same factor. This latter circumstance explains partially the resemblance of

the $0 \rightarrow \nu_{11}$ band and a parallel band of a symmetric top molecule. Further explanations require the analysis of the dependence of intensities on rotational quantum numbers provided the next section.

2. Transitions probability for localized rotational states

Consider absorption transitions involving typical quasi-degenerate rotational state doublets of type C , i.e., localized states that correspond to the precession of \mathbf{J} about axis C . As the transition moment operator, assuming that the incoming radiation is linearly polarized along the world axis Z , take the world projection \mathbf{m}_0 of $\boldsymbol{\mu}$, which is expressed as

$$\mathbf{m}_0(\alpha, \beta, \gamma; q) = \sum_{\xi=0, \pm 1} D_{\xi 0}^1(\alpha, \beta, \gamma) \mu_\xi(q).$$

Here D^1 is rank-1 Wigner's function of Euler angles, and

$$\mu_0 = i\mu_c, \quad \mu_{\pm 1} = \mp i(\mu_a \pm i\mu_b)/\sqrt{2}$$

are standard axial components of vector $\boldsymbol{\mu}$, see Ref. 67, Chapt. XIV-107,110. The transition probabilities are given by the squared absolute values of the matrix elements of $\mathbf{m}_0(\alpha, \beta, \gamma; q)$ on the vibration-rotation wavefunctions

$$|vJMk\Gamma\rangle = |v\rangle|J, M, k, \Gamma\rangle \quad \text{with } k = |m|, \quad m := J_c,$$

where $|v\rangle$ are oscillator eigenfunctions, M and m are projections of the angular momentum \mathbf{J} on the world axis Z and body axis C , respectively, while k and $\Gamma = A, B_1, B_2, B_3$ label D_2 -symmetrized rotational basis functions (Wang functions) which are used normally for asymmetric tops (see Ref. 67, Chapt. XIII-103). These functions are simple linear combinations

$$|J, M, 0\Gamma\rangle = |J, M, 0\rangle,$$

$$|J, M, k\Gamma\rangle = (|J, M, k\rangle + s_{Jk\Gamma}|J, M, -k\rangle)/\sqrt{2},$$

of standard axial rotational functions

$$|J, M, \pm m\rangle = i^J \frac{\sqrt{2J+1}}{2\pi\sqrt{2}} D_{\pm mM}^J(\alpha, \beta, \gamma),$$

for which we have (Eq. 110.6 in Ref. 67, Chapt. XIV)

$$\langle v'J'M'm'|\mathbf{m}_0|vJMm\rangle = i^{J-J'} \sqrt{(2J+1)(2J'+1)} \begin{pmatrix} J' & 1 & J \\ -M' & 0 & M \end{pmatrix} (-1)^{-M'} \sum_{\xi=0, \pm 1} (-1)^{m'} \begin{pmatrix} J' & 1 & J \\ -m' & \xi & m \end{pmatrix} \langle v'|\mu_\xi(q)|v\rangle$$

with immediate restrictions $J' = J, J \pm 1$, $M' = M$, and $m' = m + \xi$. For $\langle v' J' M' k' \Gamma' | \mathbf{m}_0 | v J M k \Gamma \rangle$ we obtain

$$\begin{aligned} \langle v' J' M' 0 \Gamma' | \mathbf{m}_0 | v J M 0 \Gamma \rangle &= \langle v' J' M 0 | \mathbf{m}_0 | v J M 0 \rangle \\ \langle v' J' M' 1 \Gamma' | \mathbf{m}_0 | v J M 0 \Gamma \rangle &= (\langle v' J' M, 1 | \mathbf{m}_0 | v J M 0 \rangle + s' \langle v' J' M, -1 | \mathbf{m}_0 | v J M 0 \rangle) / \sqrt{2} \\ &= \langle v' J' M 1 | \mathbf{m}_0 | v J M 0 \rangle \left[1 - s' (-1)^{J'+J} \right] 2^{-1/2} \\ \langle v' J' M' k' \Gamma' | \mathbf{m}_0 | v J M k \Gamma \rangle &= (\langle v' J' M k' | \mathbf{m}_0 | v J M k \rangle + s' s \langle v' J' M, -k' | \mathbf{m}_0 | v J M, -k \rangle) / 2 \\ &\quad + (s' \langle v' J' M, -k' | \mathbf{m}_0 | v J M k \rangle + s \langle v' J' M k' | \mathbf{m}_0 | v J M, -k \rangle) / 2 \\ &= \frac{1}{2} \langle v' J' M k' | \mathbf{m}_0 | v J M k \rangle \left(1 - s s' (-1)^{J'+J} \right) + \frac{1}{2} \langle v' J' M, -k' | \mathbf{m}_0 | v J M k \rangle \left(s' - s (-1)^{J'+J} \right) \\ &= \langle v' J' M k' | \mathbf{m}_0 | v J M k \rangle \left[1 - s s' (-1)^{J'+J} \right] 2^{-1} \end{aligned}$$

where $k, k' > 0$, $s := s_{Jk\Gamma}$ and $s' := s_{J'k'\Gamma'}$, and the standard property (for even J, J' , etc)

$$\sum_{\xi=0,\pm 1} (-1)^{m'} \begin{pmatrix} J' & 1 & J \\ -m' & \xi & m \end{pmatrix} = \sum_{\xi=0,\pm 1} (-1)^{-m'} (-1)^{J'+1+J} \begin{pmatrix} J' & 1 & J \\ m' & -\xi & -m \end{pmatrix} = -(-1)^{J'+J} \sum_{\xi=0,\pm 1} (-1)^{m'} \begin{pmatrix} J' & 1 & J \\ -m' & \xi & m \end{pmatrix}$$

is used. Furthermore, for all $k > 0$ the term $\langle v' J' M, -k' | \mathbf{m}_0 | v J M k \rangle$ with $m' = -k'$, $m = k$, and $m' < m + \xi$ vanishes. The sum of the squared absolute values of these matrix elements over all M accounts for the level degeneracy on J_Z and eliminates the dependence on M through $\sum_M \begin{pmatrix} J' & 1 & J \\ -M & 0 & M \end{pmatrix}^2 = \frac{1}{3}$. In particular, we obtain transition probability

$$\mathcal{P}_{v' J' m' \leftrightarrow v J m} := 3 \sum_M |\langle v' J' M' m' | \mathbf{m}_0 | v J M m \rangle|^2 = (2J+1)(2J'+1) \begin{pmatrix} J' & 1 & J \\ -m' & \xi & m \end{pmatrix}^2 |\langle v' | \mu_\xi(q) | v \rangle|^2, \quad \text{with } m' = m + \xi.$$

It can be seen that for any given $k, k' \geq 0$ the value of ξ is fixed by the selection rule $k' = \xi + k$. Furthermore, because the μ_a and μ_b components of μ_\pm are of different symmetry, only one of them is selected by the matrix element $\langle v' | \mu_\pm | v \rangle$ on vibrational states of respective symmetries $\Gamma_{v'}$ and Γ_v . Specifically,

$$|\langle v' | \mu_\pm | v \rangle|^2 = |\langle v' | \mu_a | v \rangle|^2 / 2 \text{ if } \Gamma_{v'} \neq \Gamma_v, \quad \text{and} \quad |\langle v' | \mu_\pm | v \rangle|^2 = |\langle v' | \mu_b | v \rangle|^2 / 2 \text{ if } \Gamma_{v'} = \Gamma_v.$$

Therefore, in all cases, the expression for the squared matrix element of \mathbf{m}_0 consists of a single term. Substituting expressions for the concrete Wigner $3jm$ coefficients (see Table 9 in Chap. XIV.106 of Ref. 67), we obtain the transition probabilities for specific cases

$$\begin{aligned} \mathcal{P}_{v' J' 0 \Gamma' \leftrightarrow v J 0 \Gamma} &= |\langle v' J' 0 | \mathbf{m}_0 | v J 0 \rangle|^2 = (2J+1)(2J'+1) \begin{pmatrix} J' & 1 & J \\ 0 & 0 & 0 \end{pmatrix}^2 |\langle v' | \mu_c | v \rangle|^2 \\ &= 0 \text{ for } J' = J \\ &= J |\langle v' | \mu_c | v \rangle|^2 \text{ for } J' = J - 1 \\ \mathcal{P}_{v' J' 1 \Gamma' \leftrightarrow v J 0 \Gamma} &= (2J+1)(2J'+1) \begin{pmatrix} J' & 1 & J \\ -1 & 1 & 0 \end{pmatrix}^2 \frac{1}{2} |\langle v' | \mu_{a,b} | v \rangle|^2 \frac{1}{2} \left[1 - s' (-1)^{J'+J} \right]^2 \\ &= \frac{1}{2} (2J+1) |\langle v' | \mu_{a,b} | v \rangle|^2 \text{ for } J' = J \text{ and } s' = -1 \\ &= \frac{1}{2} (J-1) |\langle v' | \mu_{a,b} | v \rangle|^2 \text{ for } J' = J - 1 \text{ and } s' = 1 \\ \mathcal{P}_{v' J' k' \Gamma' \leftrightarrow v J k \Gamma} &= (2J+1)(2J'+1) \begin{pmatrix} J' & 1 & J \\ -k' & \xi & k \end{pmatrix}^2 |\langle v' | \mu_\xi | v \rangle|^2 \frac{1}{4} \left[1 - s s' (-1)^{J'+J} \right]^2 \\ &= \frac{k^2 (2J+1)}{J(J+1)} |\langle v' | \mu_c | v \rangle|^2 \text{ for } J' = J, k' = k, \text{ and } s' = -s \\ &= \frac{J^2 - k^2}{J} |\langle v' | \mu_c | v \rangle|^2 \text{ for } J' = J - 1, k' = k, \text{ and } s' = s \\ &= \frac{(J \mp k)(J \pm k + 1)(2J+1)}{2J(J+1)} \frac{1}{2} |\langle v' | \mu_{a,b} | v \rangle|^2 \text{ for } J' = J, k' = k \pm 1 \leq J, \text{ and } s' = -s \\ &= \frac{(J \mp k)(J \mp k - 1)}{2J} \frac{1}{2} |\langle v' | \mu_{a,b} | v \rangle|^2 \text{ for } J' = J - 1, k' = k \pm 1 \leq J - 1, \text{ and } s' = s \end{aligned}$$

3. Rigid symmetric top model of intensities

Consider now the most basic imitation of DMSO using the Hamiltonian $H_{\text{rot}}^0 + H_{\text{vib}}^0$, where

$$H_{\text{rot}}^0 = \tilde{B} \mathbf{J}^2 - (\tilde{B} - C) J_c^2 \quad \text{with} \quad \tilde{B} = \frac{1}{2}(A + B) > C$$

represents a rigid symmetric top, and

$$H_{\text{vib}}^0 = \frac{\omega_{11}}{2} (p_{11}^2 + q_{11}^2) + \frac{\omega_{23}}{2} (p_{23}^2 + q_{23}^2)$$

is a simple harmonic oscillator. The intensity of the quasi-symmetric top transition $|v'J'K'\Gamma'\rangle \leftarrow |v''J''K''\Gamma''\rangle$ is given by

$$\mathcal{I} = \mathcal{P}_{v'J'K'\Gamma' \leftrightarrow v''J''K''\Gamma''} (p' - p''),$$

where the population factors in this simplest approximation can be written as

$$p' = \exp\left(-\frac{(C - \tilde{B})K'^2}{kT} - \frac{\tilde{B}J'(J' + 1)}{kT}\right)$$

with $C - \tilde{B} < 0$ for an oblate top, and

$$p'' = \exp\left(-\frac{\omega}{kT} - \frac{C - \tilde{B}}{kT}K''^2 - \frac{\tilde{B}}{kT}J''(J'' + 1)\right)$$

Continuing the symmetric top analogy, we can identify the ‘‘parallel’’ and the ‘‘perpendicular’’ (sub)bands, by $K' = K''$ and $K' = K'' \pm 1$, respectively. Recall from Sec. B 1 that the dipole moment of DMSO is far from that of a symmetric top and as a consequence, an absorption spectrum involving particular states $|v'\rangle$ and $|v''\rangle$ may consist of superimposed subbands of both types. In fact, this should be the case for $0 \rightarrow 0$ and $0 \rightarrow \nu_{11}$, and, generally, for any $\Gamma_{v'} = \Gamma_{v''}$. To understand relative intensities of *branches* within these bands, we express \mathcal{P} as function $\mathcal{P}(K, J)$ of the lower state quantum numbers $K := K'$ and $J := J'$, maximize \mathcal{I} both on K', K'' and J', J'' , and compare maximum intensities in each branch. Making estimates, we use $K, J, \Delta K = K'' - K'$, and $\Delta J = J'' - J'$. The probability \mathcal{P} and the intensity \mathcal{I} become maximal when K reaches one of the boundaries of its range $[0, J]$. To a factor, neglecting the upper state population p'' , and assuming $J \gg 1$ this gives $\mathcal{I} \approx J \exp(-\alpha J^2)$ reaching its maximum at $J_{\max} = 1/\sqrt{2\alpha}$ and where α equals either B/kT for $K \rightarrow 0$ or C/kT for $K \rightarrow J$, respectively. The value of K and the extra factor depend on the $3jm$ coefficient in $\mathcal{P}(K, J)$. Table V summarizes all concrete possibilities which we discuss in Sec. IID. Recall that in a prolate nearly symmetric top, the $K \rightarrow 0$ limit corresponds to the non-symmetric top states of type *A* and, eventually, of type *X* for the concrete case of the ν_{23} state of DMSO, while the limit of $K \rightarrow J$ represents regular symmetric top states of type *C*.

Returning to the Boltzmann factors, note that our FIR transitions at 350 cm^{-1} and 298K ($\omega/kT \approx 1.7$) require a considerable (p''/p') correction of ≈ 0.18 which should be further multiplied by

$$\exp\left(-2\Delta J \frac{B}{kT} J_{\max}\right) \exp\left(-2\Delta K \frac{C - B}{kT} K_{\max}\right)$$

to account for the rotational upper state population. Using the J_{\max} values of 21 when $K \rightarrow 0$ or 27 when $K \rightarrow J$ for DMSO at 298K , the rotational factor in p'/p'' becomes ≈ 0.95 and ≈ 1.05 for the ${}^Q R$ and ${}^Q P$ branch, respectively. As a consequence, ${}^Q R$ is about 2% more intense than ${}^Q P$ in the $0 \rightarrow \nu_{11}$ spectrum (cf Fig. 4).

TABLE V. Asymptotic (for $J \gg 1$) transition probabilities $\approx \mathcal{P}$ in the allowed branches of the vibration-rotation absorption spectrum of a nearly symmetric top molecule according to the formulae of Sec. B 2. \mathcal{P} are given without dipole moment factors, $|\langle \mu_c \rangle|^2$ and $|\langle \mu_{a,b} \rangle|^2$ for parallel (\parallel) and perpendicular (\perp) bands, respectively. The maximum \mathcal{P}_{\max} occurs for the value K_{\max} of the lower state quantum number $K \in [0, J]$; the respective maximum intensity \mathcal{I}_{\max} is achieved for the value J_{\max} (obtained in the simplest rigid body approximation) of the lower state angular momentum quantum number J . Where necessary, notably for ${}^P R, {}^R P$ and ${}^P, {}^R Q$, different values of \mathcal{P}_{\max} are given for zero K and for small $K \rightarrow 0_+$; the respective two kinds of spectral lines can be well seen in Fig. 4, left.

Branch	ΔJ	ΔK	$\approx \mathcal{P}_{K,J}$	K_{\max}	$\approx \mathcal{P}_{\max}$	$\approx \mathcal{I}_{\max}^2$
\parallel ${}^Q Q$	0	0	$\frac{2K^2}{J}$	J	$2J$	$\frac{kT}{2C}$
\parallel ${}^Q R, {}^Q P$	± 1	0	$\frac{J^2 - K^2}{J}$	0	J	$\frac{kT}{2B}$
\perp ${}^P Q, {}^R Q$	0	± 1	$\frac{J^2 - K^2}{2J}$	0_+	$\frac{J}{2}$	$\frac{kT}{2B}$
				0	J	$\frac{kT}{2B}$
\perp ${}^P R, {}^R P$	± 1	∓ 1	$\frac{(K - J)^2}{4J}$	0_+	$\frac{J}{4}$	$\frac{kT}{2B}$
				0	$\frac{J}{2}$	$\frac{kT}{2B}$
\perp ${}^R R, {}^P P$	± 1	± 1	$\frac{(K + J)^2}{4J}$	J	J	$\frac{kT}{2C}$

Appendix C: Bifurcation of the rotational energy

Consider an effective rotational Hamiltonian H_{rot} reduced to Watson’s D_2 -symmetric *s*-form^{30,39}. This Hamiltonian describes rotational energy levels of a nondegenerate isolated vibrational state of a nearly symmetric top molecule. Its classical analog $\mathcal{H}_{\text{rot}} : \mathbb{S}_j^2 \rightarrow \mathbb{R}$ is function of spherical coordinates (θ, φ) and parameter $j > 0$ (see Sec. IC), whose order $(n - 1)$ is a linear combination of terms of two kinds, specifically

$$j^{2n} \cos(\theta)^{2k} \text{ with } n \geq k \geq 0,$$

which come from the diagonal operators $J^{2(n-k)} K^{2k}$, and

$$2j^{2n} \sin(\theta)^{2l} \cos(2l\varphi) \text{ with } n \geq l \geq 1,$$

which correspond to the $J^{2(n-l)}(J_+^{2l} + J_-^{2l})$ tensors. Thus, in particular, we have

$$\begin{aligned} j^{-2}\mathcal{H}_{\text{rot}}^{(0)} &= \frac{1}{2}(A + B) + \left[C - \frac{1}{2}(A + B)\right] \cos(\theta)^2 \\ &\quad + \frac{1}{2}(A - B) \sin(\theta)^2 \cos(2\varphi), \\ j^{-4}\mathcal{H}_{\text{rot}}^{(1)} &= -D_J - D_{JK} \cos(\theta)^2 - D_K \cos(\theta)^4 \\ &\quad + 2d_1 \sin(\theta)^2 \cos(2\varphi) + 2d_2 \sin(\theta)^4 \cos(4\varphi). \end{aligned}$$

1. Consequences of symmetry

Notice that \mathcal{H}_{rot} is invariant under the operations in the $D_2 \times \mathcal{T}$ group, which is D_2 extended by the momentum (or time) reversal \mathcal{T} , and which acts on \mathbb{R}_j^3 with coordinates (j_a, j_b, j_c) , and on the phase space \mathbb{S}_j^2 embedded in \mathbb{R}_j^3 , as a point group D_{2h} . The presence of this symmetry helps finding equilibria of the system⁶⁹ (stationary points of H_{rot}). Under the action of $D_2 \times \mathcal{T}$, the space \mathbb{S}_j^2 becomes inhomogeneous. The intersections of \mathbb{S}^2 with principal axes j_a , j_b , and j_c correspond²³ to three isolated two-point orbits $\{\theta = \pi/2, \varphi = \pm\pi/2\}$, $\{\theta = \pi/2, \varphi = 0, \pi\}$, and $\{\theta = 0, \pi\}$, respectively, which must be stationary points of H_{rot} . The planes $\sigma = \sigma_{AC}$, σ_{BC} , and the equatorial plane σ_{AB} have nontrivial stabilizers in the class $C_s \subset C_2 \times \mathcal{T} \subset D_2 \times \mathcal{T}$. As a consequence, the gradient $\nabla \mathcal{H}_{\text{rot}}$ on $\sigma \cap \mathbb{S}_j^2$ remains in the plane σ (and tangent to \mathbb{S}^2). This means that *typically*, i.e., for all values of j on an open nonzero interval $(j'_{\text{crit}}, j''_{\text{crit}}) \subset \mathbb{R}_{>0}$, the equilibria would lie in one of $\sigma \cap \mathbb{S}_j^2$ because on σ , equations $\nabla \mathcal{H}_{\text{rot}} = 0$ reduce to one scalar equation and can be potentially satisfied for some $j \in (j'_{\text{crit}}, j''_{\text{crit}})$. Because $D_2 \times \mathcal{T}$ acts nontrivially on $\sigma \cap \mathbb{S}^2$, the equilibria on $\sigma \cap \mathbb{S}^2 \setminus \{\text{fixed points}\}$ should form a four-point orbit which corresponds to two equivalent axes of stationary rotation lying in σ . Finally note that existence of other, exceptional roots of $\nabla \mathcal{H}_{\text{rot}}$ may indicate the limitation of the isolated vibrational state model, and/or of the s -reduction scheme, which relies on the near-symmetric-top assumption.

2. Stationary points

Computing ∇H_{rot} provides concrete information on the equilibria of the system. The first derivative $\partial \mathcal{H}_{\text{rot}} / \partial \theta$ is a linear combination of

$$-k j^{2n} \sin(2\theta) \cos(\theta)^{2k-2} \text{ with } k = 1, 2, \dots, n$$

and

$$2l j^{2n} \sin(2\theta) \sin(\theta)^{2l-2} \cos(2l\varphi) \text{ with } l = 1, 2, \dots, n,$$

while $\partial H_{\text{rot}} / \partial \varphi$ has terms of just one kind

$$-4l j^{2n} \sin(\theta)^{2l} \sin(2l\varphi) \text{ with } n \geq l \geq 1.$$

We see that $\partial \mathcal{H}_{\text{rot}} / \partial \varphi$ vanishes on σ_{AC} and σ_{BC} , where φ is 0 and $\pi/2$, respectively, and that $\partial \mathcal{H}_{\text{rot}} / \partial \theta$ vanishes on σ_{AB} , where $\theta = \pi/2$, and on axis j_c , i.e., on $\sigma_{AC} \cap \sigma_{BC}$ with $\theta = 0$. This confirms all statements in Sec. C1.

Considering the concrete values of the rotation constants A , B , and C , we can observe that, as long as $(A+B)/2$ differs significantly from C , and is much larger than $(A-B)/2$, i.e., near the limit of a well pronounced symmetric top, additional equilibria on the meridian

planes σ_{AC} and σ_{BC} are very unlikely to exist at reasonable values of j . So we concentrate on the equator $\sigma_{AC} \cap \mathbb{S}_j^2$, where the equations $\nabla \mathcal{H}_{\text{rot}} = 0$ reduce to

$$-(2j)^{-2} (\partial H_{\text{rot}} / \partial \varphi) = \sum_{n=1}^n \sum_{l=1}^n c_{l,n} l j^{2n-2} \sin(2l\varphi) = 0$$

with coefficients $c_{l,n}$ given by the parameters of \mathcal{H}_{rot} (see Table I). Using Chebyshev polynomials U_i of the second kind, we express

$$\sin(2l\varphi) = \sin(2\varphi) U_{l-1}(\cos(2\varphi)) = \sin(2\varphi) \mathcal{P}_l(\cos \varphi)$$

where $\mathcal{P}_l(x)$ with $x \in [-1, 1]$ is a sum of even degree Chebyshev polynomials $T_{2i}(x)$ of the first kind,

$$\mathcal{P}_l(x) = \begin{cases} 2 \sum T_{2i}(x), & i = 1, 3, \dots, l-1 \text{ for even } l, \\ 2 \sum T_{2i}(x) - 1, & i = 0, 2, \dots, l-1 \text{ for odd } l. \end{cases}$$

Factoring out $\sin(2\varphi)$ in order to exclude the trivial roots $\varphi = 0, \pi/2$, etc at axes j_b and j_a , we obtain the final form of the equation for the nontrivial equilibria with $\theta = \pi/2$

$$\mathcal{F}(x, j) := \sum_{n=1}^n \sum_{l=1}^n c_{l,n} l j^{2n-2} \mathcal{P}_l(x) = 0 \text{ with } x \in [-1, 1].$$

Direct computation with $n \leq 3$ gives

$$\begin{aligned} \mathcal{F}(x, j) = & A - B + 4(4d_2 - d_1 - 8d_2 x^2) j^2 \\ & + 4(-48h_3 x^4 + 8(6h_3 - h_2) x^2 - (9h_3 - 4h_2 + h_1)) j^4 \\ & + \dots \end{aligned}$$

where parameters A , B , d , etc refer to a particular vibrational state, cf Table I. Since $\mathcal{F}(x, j)$ is a polynomial in $x^2 \in [0, 1]$ (and j^2) these equilibria come in pairs. The operation $x \rightarrow -x$ corresponds in \mathbb{R}_j^3 to the C_2 rotation about axis j_a (point $x = 0$) and so any two points $\pm x$ represent two equivalent axes of rotation (cf Sec. C1).

3. Critical values of j

If for some $j > 0$, $\mathcal{F}(x, j) = 0$ is satisfied for some $x_0^2 \in (0, 1)$ then, by continuity, it is satisfied for j and x^2 on nonzero intervals $(j'_{\text{crit}}, j''_{\text{crit}}) \subset \mathbb{R}_{>0}$ and $((x')^2, (x'')^2) \subset (0, 1)$, respectively. One possibility for the nontrivial roots x_0 to appear or disappear is to enter or exit $[0, 1]$. In this case, the stationary point of H_{rot} at one of the endpoints of $[0, 1]$ is degenerated and we have a pitchfork bifurcation (bifurcation with broken symmetry of order two). Solving equations $\mathcal{F}(x, j)|_{x=0} = 0$ and $\mathcal{F}(x, j)|_{x=1} = 0$ gives corresponding critical values j_{crit} marking the bifurcation of axis j_a (with $\varphi = \pi/2$) and j_b , respectively. Checking Table I and taking into account that $-d_2 \gg d_1 > 0$ for ν_{23} of DMSO while $A > B$, we can see that the bifurcation occurs at $x = 0$, and that in the simplest approximation,

$$j_{\text{crit}}^2 = \frac{1}{4} \frac{A - B}{d_1 - 4d_2}.$$

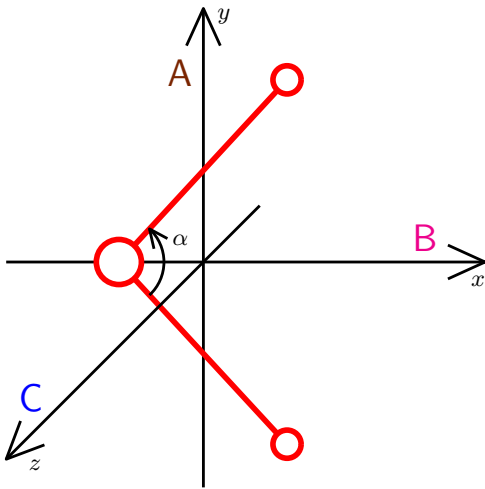


FIG. 17. Schematic representation of the equilibrium configuration of an AB_2 molecule and its principal axes of inertia. Assuming that AB_2 correspond to SC_2 in DMSO, the orientation and notation of the axes agrees with that in Fig. 1.

Appendix D: Stationary axes of rotation of a symmetric nonlinear molecule AB_2 in the rigid bender model

To facilitate the comparison to the case of DMSO, we give a brief outline of the approach in Refs. 11, 48, 50. For the coordinate axes chosen as shown in Fig. 17, the principal moments of inertia of the AB_2 molecule of total

mass $M = 2m_B + m_A$ are

$$\begin{aligned} I_x &= 2m_B|AB|^2 \sin(\alpha/2)^2, \\ I_y &= 2m_B|AB|^2 \cos(\alpha/2)^2 \frac{m_A}{M}, \\ I_z &= I_x + I_y, \end{aligned}$$

where $\alpha < \pi$ is the angle BAB . It follows that for all $\alpha > \alpha_{\text{crit}}$ we have $I_z > I_x > I_y$. The respective principal axes C , B , and A are similar to those of DMSO, where AB_2 can be seen as the $S(\text{CH}_3)_2$ fragment (cf Figs. 17 and 1). Furthermore, like in the case of DMSO, it is A (axis y) that undergoes the pitchfork bifurcation.

The critical value α_{crit} , for which the two moments of inertia I_x and I_y become equal, is given by

$$\tan(\alpha_{\text{crit}}/2)^2 = \frac{m_A}{M} < 1.$$

In general $\alpha_{\text{crit}} < \pi/2$; when $m_A \gg m_B$, such as in the $H_2\text{Se}$ molecule^{14,15,54,55}, α_{crit} approaches $\pi/2$.

With all vibrations ignored (frozen), we can write the classical rotational energy

$$\mathcal{H}_{\text{rot}} = \min_{\alpha} \left[\frac{j_z^2}{2I_z} + \frac{j_x^2}{2I_x} + \frac{j_y^2}{2I_y} + \frac{1}{2}k(\alpha - \alpha_0)^2 \right],$$

where α_0 is the equilibrium angle for $j = 0$, and k is the harmonic force constant of the bending vibration; typically we expect $\alpha_0 > \alpha_{\text{crit}}$. Subsequently, \mathcal{H}_{rot} can be investigated as outlined in Sec. IC and III, and Appendix C. In particular, it can be shown that for rotations about y (axis A), i.e., when $j_x^2 + j_z^2 \ll j^2$, the angle $\alpha(j)$, that minimizes the energy of rotation, becomes smaller than α_0 . This is the obvious consequence of the centrifugal forces created by rotation about axis A . So for α_0 sufficiently close to $\alpha_{\text{crit}} < \alpha_0$ and sufficiently large j , we can achieve $\alpha(j) \approx \alpha_{\text{crit}}$. Furthermore, this model reproduces the pitchfork bifurcation of axis A in which A becomes unstable and two new equivalent axes X appear.